Accretion of Ornamental Equatorial Ridges on Pan, Atlas and Daphnis

Alice C. Quillen[a,*], Fatima Zaidouni[a], Miki Nakajima[a,b], Esteban Wright[a]

[a]*Department of Physics and Astronomy, University of Rochester, Rochester, NY 14627 USA*
[b]*Department of Earth and Environmental Sciences, University of Rochester, Rochester, NY 14627, USA*

Abstract

We explore scenarios for the accretion of ornamental ridges on Saturn's moons Pan, Atlas, and Daphnis from material in Saturn's rings. Accretion of complex shaped ridges from ring material should be possible when the torque from accreted material does not exceed the tidal torque from Saturn that ordinarily maintains tidal lock. This gives a limit on the maximum accretion rate and the minimum duration for equatorial ridge growth. We explore the longitude distribution of ridges accreted from ring material, initially in circular orbits, onto a moon that is on a circular, inclined or eccentric orbit. Sloped and lobed ridges can be accreted if the moon tidally realigns during accretion due to its change in shape or because the disk edge surface density profile allows ring material originating at different initial semi-major axes to impact the moon at different locations on its equatorial ridge. We find that accretion from an asymmetric gap might account for a depression on Atlas's equatorial ridge. Accretion from an asymmetric gap at orbital eccentricity similar to the Hill eccentricity, might allow accretion of multiple lobes, as seen on Pan. Two possibly connected scenarios are promising for growth of ornamental equatorial ridges. The moon migrates through the ring, narrowing its gap and facilitating accretion. The moon's orbital eccentricity could increase due to orbital resonance with another moon, pushing it into its gap edges and facilitating accretion.

Keywords: Saturn, satellites – Rotational dynamics – Satellites, dynamics Satellites, shapes

1. Introduction

Toward the end of the Cassini mission, the spacecraft made a series of close approaches to Saturn's rings that included flybys of moons Pan, Daphnis, Pandora, Atlas, and Epimetheus. The images taken from these close approaches increasingly revealed that the small inner moons of Saturn have irregular and intricate shapes (Thomas, 2010; Thomas et al., 2013; Buratti et al., 2019; Thomas and Helfenstein, 2020). We focus here on three moons with intricate equatorial ridges, dubbed 'accretion ornaments' (Charnoz et al., 2007). Pan has a sharp edged 'ravioli'-shaped equatorial ridge, Atlas has a thin, lens-shaped equatorial ridge with a depression on one side. Daphnis is elongated and two or three two narrow ridges cross its body (see Figure 1).

The surfaces of Pan's and Atlas' equatorial ridges are smoother than the more rounded central or core components of each moon which show grooves or fractures (Buratti et al., 2019; Thomas and Helfenstein, 2020). This may also be true on Daphnis but the spatial resolution of the Daphnis imagery is poorer than that of Pan and Atlas, so it is more difficult to determine whether Daphnis' ridges are comprised of material similar to its underlying core. The central core components exhibit more impact craters than do the equatorial ridges on Pan and Atlas, which

nevertheless display a few sub-kilometer impact craters (Buratti et al., 2019). At high and low latitudes, Pan's core appears bare of loose material. In contrast, Atlas's core seems covered by about ten meters of loose material which has been called 'icy regolith' (Buratti et al., 2019). Pan's equatorial ridge encircles its equator and resembles a polygon (Buratti et al., 2019; Thomas and Helfenstein, 2020).

The shapes of Pan and Atlas are not close to gravitational equilibrium figures or Roche ellipsoids (Porco et al., 2007; Thomas and Helfenstein, 2020). These moons are not spinning fast enough to form a diamond or top shape like some asteroids (e.g., asteroid 1999 KW4; Ostro et al. 2006). Tidal stress due to Saturn can deform a moon, altering its surface morphology (Buratti et al., 2019). However, tidal stress would elongate a synchronously rotating body in the radial direction (along the moon-Saturn line) rather than create a thin equatorial ridge. Neither centrifugal nor tidal forces alone can account for all aspects of the equatorial ridge morphology (e.g., see discussion by Charnoz et al. 2007; Leleu et al. 2018; Thomas and Helfenstein 2020). Using SPH simulations, Leleu et al. (2018) showed that the spectrum of shapes of Saturn's small moons is a natural outcome of slow merging collisions. Head-on mergers result in flattened objects with equatorial ridges, like Atlas and Pan, whereas with more oblique impact angles, mergers result in elongated bodies like Prometheus (Leleu et al., 2018). However mergers

---

*Corresponding author

are unlikely to account for the differing core and ridge surface morphologies. The equatorial ridges most likely formed through slow accretion of ring particles (Charnoz et al., 2007) and both slow impacts and subsequent accretion could have taken place.

Cross sections of Pan's and Atlas' equatorial ridges are shown in Figure 9 by Thomas and Helfenstein (2020). Pan's ridge has a maximum width, measured in the direction perpendicular to its equator, of about 6 km. However PIA images N1867606181 and N1867606643 of Pan (see Figure 7 by Thomas and Helfenstein 2020) show that the ridge's outer edge is quite sharp and less than 1 km thick. Most of Altas' ridge (between 180 and 360° W longitude, as shown in the map in Figure 10 by Thomas and Helfenstein 2020) is less than 8 km thick. Daphnis' ridges, as delineated in Figure 3B by Buratti et al. (2019), have width less than 1/2 km thick. Ridges with sharp edges would be consistent with formation via accretion from fine low inclination ring material (Charnoz et al., 2007). The widths of these equatorial ridges are consistent with the low moon orbital inclinations and deposition from ring particles with height distribution in the rings near these moons (see Table 4 and associated discussion by Thomas and Helfenstein 2020). Images of Pan in Figure 1 and in the supplements by Thomas and Helfenstein (2020) show that its equatorial ridge exhibits thickness variations but suggest that the equatorial ridge on Pan is not warped. There are only a few high resolution images of Pan taken when the spacecraft was nearby so it is difficult to determine whether thickness variations are similar or different on each lobe.

Recent measurements of Pan's, Daphnis', and Atlas' orbital elements, mass, density, orbital period, and body semi-major axes (Porco et al., 2007; Jacobson et al., 2008; Buratti et al., 2019) are compiled in Table 1. We also list the volume of the equatorial ridge divided by total moon volume, f_v, estimated by Buratti et al. (2019) and Thomas and Helfenstein (2020).

All three moons lie within Saturn's main rings. Daphnis orbits Saturn in the Keeler Gap which has a half-width of 21 km and lies within the A ring. Pan, also in the A-ring, is found in the Encke Gap (Showalter, 1991) which has a half-width of 161 km. Atlas lies outside the A-ring in the Roche Division. The gravitational field of Saturn itself dominates the orbital motions of these moons and a precessing Keplerian ellipse gives an adequate model for their orbits (Jacobson et al., 2008). Atlas has a significant orbital eccentricity and inclination compared to the lower values for Pan or Daphnis, and this is due to gravitational perturbations from Prometheus and Pandora (Spitale et al., 2006; Cooper et al., 2015).

Prior work on accretion onto moons in ring systems includes a numerical study of accretion onto embedded moonlets where the moonlet's Roche lobe remains filled with accreted material (Yasui et al. 2014; also see Figure 4 by Porco et al. 2007). Here a 'moonlet' is a body with Hill radius less than a kilometer that is not massive enough to open a gap in the ring (Bromley and Kenyon, 2013).
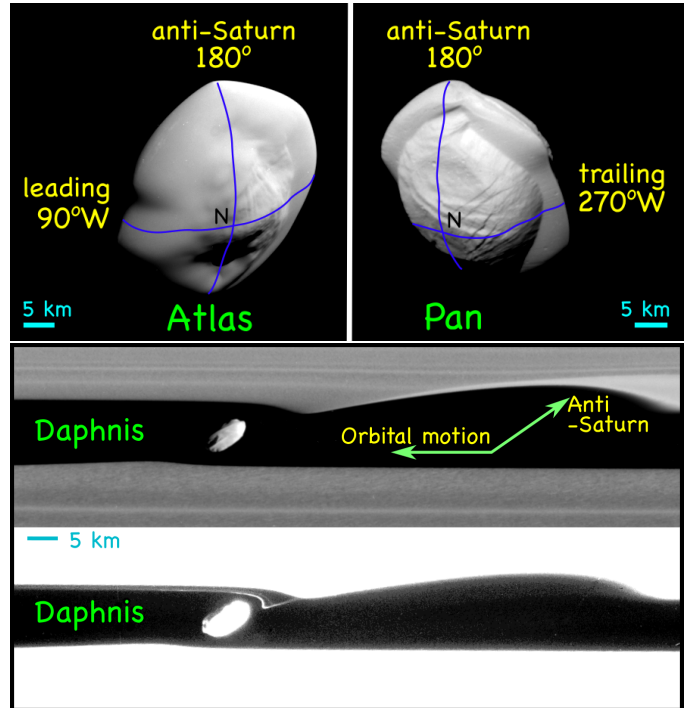

Figure 1: Grayscale images of the moons Pan, Atlas, and Daphnis obtained with ISS (the Imaging Science Subsystem) during the late Cassini mission flybys. The image numbers are N1867604669 for Pan, N1870699120 for Atlas, and N1863267232 for Daphnis. Cyan bars show 5 km distances. We labelled longitudes with blue lines on Pan and Atlas using the wire frame figures by Thomas and Helfenstein (2020) as a guide. These are shown in their Figures 7 and 8, and derived from their shape models. Convention is that 0° longitude on the moon faces Saturn and 90° W faces the direction of the moon's orbital motion. The north poles, labelled 'N' on Pan and Atlas are located where the two blue lines cross. The bottom two panels show the same image of Daphnis, but with different contrasts The bottom image better shows a faint wisp interior to the ring edge of material that was perturbed by Daphnis. These moons nearly fill their Roche region. Body axis ratios are listed in Table 1.

Pan, Atlas and Daphnis are large enough to open gaps in the ring, so we refer to them as moons rather than moonlets. Charnoz et al. (2007) proposed that accreting ring material would primarily flow through Pan's L1 or L2 Lagrange points onto Pan where it would impact the moon equator preferentially on Pan's Saturn-facing and anti-Saturn sides. Charnoz et al. (2007) proposed that the divots in Atlas's equatorial ridge are caused by its orbital eccentricity. In their numerical simulations of an accreting moon on eccentric orbit, more accreting material hit the surface on the moon's leading side than on the trailing side.

Pan's remarkable 5 or 6 pointed ravioli-shaped equatorial ridge has remained a curiosity. Likewise the multiple ridges crossing Daphnis lack a dynamical explanation. In this study we explore processes that might cause accreting ring material to pile up at particular longitudes on a moon's equator. We follow the model for equatorial ridge formation proposed by Charnoz et al. (2007), where the equatorial ridge grows via slow accretion from ambient ring material. We do not pursue alternate possible scenarios for equatorial ridge growth, such as those involving a minor merger (Leleu et al., 2018) or an accretion disk that falls back onto the moon equator (e.g., relevant for Iapetus; Ip 2006; Stickle and Roberts 2018).

In section 2 we estimate torques on the three moons. Accretion scenarios are sensitive to orbital eccentricity, so we discuss orbital eccentricity damping via driving of spiral density waves in section 3. In section 4 we examine the impact angle of material accreting from a cold ring onto a moon that is in a circular orbit. We also explore the morphology of an equatorial ridge that is accreted while tidally locked and from material that impacts the moon surface at a single impact angle. We discuss accretion from the edge of a gap in the ring, with gap edge described with a surface density profile. In section 5 we examine the distribution of impact angles for material accreting from a ring onto a moon that is in an eccentric orbit. Scenarios for equatorial ridge accretion are discussed in section 6. A summary and discussion is in section 7. Appendix A describes additional details used in our illustrative toy models.

2. Tidal and accretion torques

We consider a moon that is accreting from a stream of material that impacts its surface. If the accretion stream impacts the moon tangentially, (it approaches on a non-radial trajectory with respect to the moon's center of mass), then the accreting material exerts a torque on the moon that can perturb the moon's spin rate and orientation. Saturn's regular moons are in spin-synchronous or tidally locked states due to the tidal torque exerted on them by Saturn. We estimate the torque on an initially spinning moon and the time it takes to reach tidal lock via internal dissipation. We compare the tidal torque to the torque that could arise from accretion. If the torque from accreting material is high enough, it would pull the moon out of the spin-synchronous state.

2.1. Tidal torque

The secular part of the semi-diurnal ($l = 2$) term in the Fourier expansion of the perturbing potential from point mass M_*, gives a tidally induced torque on an extended body of mass M

$$T_2 = \frac{3}{2} \frac{GM_*^2}{a} \left(\frac{R}{a}\right)^5 k_2 \sin \epsilon_2, \tag{1}$$

where $k_2 \sin \epsilon_2$ is known as the quality function, describing deformation and dissipation in M (e.g., Kaula 1964; Goldreich 1963; Efroimsky and Makarov 2013). The quality function is often approximated as k_2/Q where Q is a dissipation factor for mass M that is commonly called the 'Quality factor'. The Love number k_2 characterizes tidal deformation of M. Here a is the orbital semi-major axis of M about M_*, R is the radius of mass M, assumed spherical, and G is the gravitational constant. The torque causes the spin ω of M to vary. The torque can be used to estimate a time t_{despin} for a spherical body to spin up or down from an initial spin rate of ω_0 to the tidally locked state. Assuming an initial spin rate near centrifugal break-up $\omega_0 = \sqrt{GM/R^3}$,

$$t_{despin} \sim \frac{\omega_0}{\dot{\omega}} \sim \frac{2P}{15\pi} \left(\frac{M}{M_*}\right)^{\frac{3}{2}} \left(\frac{a}{R}\right)^{\frac{9}{2}} \frac{Q}{k_2}, \tag{2}$$

where P is the initial orbital period. We use this time to characterize the rate that a moon's spin varies when it is not in a spin-synchronous (tidally locked) state or within a spin-orbit resonance. For estimates of this time scale, we adopt Love number $k_2 = 0.038 e_g/\mu_{shear}$ (consistent with the derivation by Frouard et al. 2016 for a homogeneous viscoelastic sphere) where gravitational binding energy $e_g \equiv GM^2/R^4$ and μ_{shear} is the shear modulus of mass M's interior. We adopt $\mu_{shear} Q = 10^{11}$ Pa typical of ice or rubble (Pravec et al., 2014). This value is consistent with $\mu_{shear} = 10^9$ Pa and $Q = 100$. The tidal spin-down times for the three moons are computed from values listed in Table 1 for the three moons and are listed in Table 2. The spin-down times, $\sim 100,000$ yr, are short compared to the age of the Solar system, but are long compared to the orbital periods of Saturn's regular moons.

2.2. Torque from accretion

If a moon is accreting mass at a rate $\dot{M}$, approximately what is the torque on the moon? The L1 or L2 Lagrange equilibrium points are about 1 Hill radius $R_H = a(\mu/3)^{\frac{1}{3}}$ away from the moon center of mass. Here $\mu \equiv M/M_*$ is the ratio of moon to planet mass. To estimate the torque, we consider the spin angular momentum imparted to the moon by the impact of an unperturbed test particle in an initially coplanar, circular orbit about the planet. A test

particle that is in a circular orbit at semi-major axis of $a' = a + \Delta a$ with separation $\Delta a = R_H$ has mean motion $n' = n + \frac{dn}{da}R_H$. The difference in mean motion between test particle and moon $\delta n = \frac{dn}{da}R_H = \frac{3}{2}n\frac{R_H}{a}$ (and we are ignoring the sign of our estimate). The tangential velocity component (computed using the origin at the moon's center of mass) of the test particle is $v_\theta \sim a\delta n \sim \frac{3}{2}v_H$ where $v_H \equiv nR_H$ is the Hill velocity. If this particle hits and sticks to the moon, the change in spin angular momentum of the moon per unit accreted mass would be

$$\delta l \sim R_H v_\theta \sim \frac{3}{2}v_H R_H \sim \frac{3}{2}nR_H^2. \tag{3}$$

The torque on the moon due to accreting material is approximately

$$T_{\rm acc} \sim \frac{3}{2}\dot{M}nR_H^2. \tag{4}$$

Below we integrate orbits that impact a moon (sections 4 and 5) to improve upon this torque estimate.

The torque from accreting material can vary the moon's spin, possibly even pulling it out of the spin synchronous state if the accretion rate is high enough. What accretion rate is large enough for the torque from accreting material to exceed the spin-down tidal torque from Saturn on the moon?

The ratio of the torque from accreting material (equation 4) to that caused by Saturn's tide (if not tidally locked; equation 1) is

$$\frac{T_{\rm acc}}{T_2} \sim \frac{\dot{M}}{Mn}\left(\frac{M}{M_*}\right)^{\frac{5}{3}}\left(\frac{a}{R}\right)^5\left(\frac{Q}{k_2}\right)3^{-\frac{2}{3}}, \tag{5}$$

where we have replaced the quality function with k_2/Q. We recognize an accretion time scale $t_{\rm acc} \equiv M/\dot{M}$. In Table 2 we include values for the torque ratio $\frac{T_{\rm acc}}{T_2}\frac{Mn}{\dot{M}}$ computed for the three moons using dissipation factor Q and Love number k_2 computed with $\mu_{\rm shear}Q = 10^{11}$ Pa as previously described in section 2.1.

When the torque from accreting material exceeds the tidal torque from Saturn, the moon would be pulled out of a tidally locked spin synchronous state or a spin-orbit resonance. What mass accretion rate is sufficient to allow this to happen? We set $T_{\rm acc} = T_2$, balancing accretion with tidal torque, and solve equation 5 for a critical accretion $\dot{M}_{cr}$

$$\dot{M}_{cr} = Mn\left(\frac{M_*}{M}\right)^{\frac{5}{3}}\left(\frac{R}{a}\right)^5\left(\frac{k_2}{Q}\right)3^{\frac{2}{3}}. \tag{6}$$

Critical values of the accretion rate are listed in Table 2 for the three moons and are approximately $\dot{M}_{cr} \sim 10^{10}$ kg/yr. We also include in Table 2 estimates for an accretion timescale at this rate of the equatorial ridges $Mf_v/\dot{M}_{cr}$ (where f_v is the fraction of volume in the ridge).

Accretion rates above $\dot{M}_{cr}$ would be large enough to pull the moon out of the spin synchronous state and in that case we would expect smooth equatorial ridges that lack divots or polygon shapes. As the equatorial ridges in Pan and Atlas have non-axisymmetric structure, we would infer that the accretion rates during equatorial ridge formation were lower than the critical ones. We estimate that the time over which accretion took place was longer than the time scale $Mf_v/\dot{M}_{cr}$ which is of order 10^5 years for these moons (see Table 2). This implies that the duration for accretion of these equatorial ridges was probably longer than about 10^5 years.

We compare the critical accretion rate to viscous accretion rate through the A ring. Using a ring viscosity of $\nu = 64$ cm^2/s in the A-ring near Pan (Tajeddine et al., 2017a), and a ring mass surface density of $\Sigma_{\rm ring} \approx 40$ g/cm^2 (Tiscareno et al., 2007), the viscous accretion rate through the ring at Pan's orbital semi-major axis $\dot{M}_{\rm cross} \sim 3\pi\Sigma_{\rm ring}\nu \sim 10^9$ kg/yr. Our estimate for the critical value $\dot{M}_{cr}$ is above this value, so if accretion onto Pan is fed purely by viscous accretion in a ring edge we could expect accretion to take place below the critical accretion rate $\dot{M}_{cr}$.

A larger rate of mass could cross the moon's orbit if the moon migrates. Bromley and Kenyon (2013) estimate that Pan and Daphnis have masses in the range that allows rapid migration to occur, at about $\frac{da_{\rm mig}}{dt} \sim 20$ km/yr. Rapid or type III migration occurs when orbit crossing material exchanges angular momentum with a planet or moon near the ends of horseshoe orbits (Masset and Papaloizou, 2003). A condition for rapid or runaway migration, via a type III mechanism involving co-orbital material (Masset and Papaloizou, 2003), is proximity to dense ring material with a low dispersion of eccentricity. At a migration rate of $\frac{da_{\rm mig}}{dt} \sim 20$ km/yr, a mass rate of $\dot{M}_{\rm cross} = 2\pi\Sigma_{\rm ring}a\frac{da_{\rm mig}}{dt} \sim 7 \times 10^{15}$ kg/yr crosses the moon's orbit as it drifts through the ring, vastly exceeding the critical rate, $\dot{M}_{cr}$. Most of this material would cross the moon's orbit from one side to the other side rather than be accreted onto the moon. Such a high migration rate cannot be maintained in the same direction for long (or even long enough to accrete the equatorial ridges), otherwise the moons would have left the ring. The two mass rates for $\dot{M}_{\rm cross}$ (estimated via viscous evolution and via rapid migration) bracket the possible accretion rates during formation of these equatorial ridges.

In summary, we estimate the torque on a moon due to angular momentum in accreting material and we compare this torque to the tidal torque exerted by Saturn. This accretion torque lets us estimate a critical accretion rate that would be large enough to pull the moon out of a tidally locked state or a spin-orbit resonance. If the moon is not tidally locked (or in a spin-orbit resonance), then we would expect accretion to be evenly distributed around the equator, giving a ridge that lacks divots or radial extensions. As both Pan and Atlas's ridges have non-axisymmetric structure, we infer that the accretion rates of their ridges primarily occurred at rates below M_{cr} which we estimate is

of order 10^{10} kg/yr. The accretion rate during much of the formation of Pan's, Atlas' and Daphnis' equatorial ridges was likely below 10^{10} kg/yr and took place in a nearly tidally locked setting and with duration longer than about 10^5 years. We return to possible connections between disk evolution, moon migration and equatorial ridge accretion in section 6.

3. Eccentricity damping via driving spiral density waves

The orbital eccentricity of a moon affects its mode of accretion from ring material (Charnoz et al., 2007). The eccentricity of a tidally locked body in eccentric orbit (following Peale and Cassen 1978; Yoder 1982) is damped. With tidal torque alone, it would take longer than about 10^{12} years for the orbital eccentricity of these moons to decay. However, the torque from driving spiral density waves into the ring exceeds the tidal torque.

Hahn (2008) estimated the time for Pan's eccentricity to damp due to spiral density waves driven by Pan into the ring material interior and exterior to Pan. With the current Encke gap width (with a half-width $\Delta a/R_H \approx 8.45$), Hahn (2008) finds an eccentricity damping time $\tau_e = \dot{e}/e \sim 2000$ years. N-body simulations of a Pan- or Daphnis-sized moon in proximity to a particulate disk show rapid eccentricity damping in about 100 years (Bromley and Kenyon, 2013), supporting the short time estimated by Hahn (2008). The eccentricity damping time is short, suggesting that Pan's orbital eccentricity should be extremely small. Pan's current non-zero eccentricity can be attributed to a nearby 16:15 inner mean motion resonance with Prometheus (Spitale et al., 2006; Hahn, 2008). Because of the short estimated eccentricity damping time, it would be difficult to maintain Pan's eccentricity over 10^5 years (so that it remains tidally locked during ridge accretion) unless Pan's eccentricity were resonantly excited by another moon.

Pan is inside the orbit of Prometheus. If Pan's orbital semi-major axis were only 31 km lower, it would be strongly perturbed by the 16:15 resonance with Prometheus. Pan's orbital migration is currently thought to be prevented by resonant excitations and orbital stirring of the ring material by other moons (Bromley and Kenyon, 2013). However, it is likely that Pan and other moons have migrated in the past (Bromley and Kenyon, 2013). Pan's eccentricity could have been excited in the past, possibly for long periods of time, if it remained in an orbital resonance with another moon.

Atlas, since it currently resides outside the A ring (43 Hill radii away from the edge), primarily drives spiral density waves distant from itself and so should have a significantly longer eccentricity damping timescale. However, during an epoch when it accreted ring material, it too could have required eccentricity excitation to maintain its eccentricity.

Damping times for Pan's and Daphnis' orbital inclination via excitation of density waves are estimated to be similar in duration as those for eccentricity damping (Hahn, 2008; Weiss et al., 2009).

4. Test particles that impact a moon in a circular orbit

In this section we discuss the trajectories of particles that impact a moon that is in a circular orbit. This is a fiducial case, but this case may also be relevant for accretion while a moon is migrating through a disk. In that setting the moon may reside within a narrow gap. A stream of fresh ring material can continually approach the moon (e.g., see Figure 4 by Bromley and Kenyon 2013 showing an N-body simulation of a Daphnis-sized moon undergoing rapid migration through a particle disk).

We refer to massless particles as test particles. We integrate test particle orbits using the N-body code re-bound (Rein and Liu, 2012) and with the 15-order adaptive step size integrator known as 'IAS15' (Rein and Spiegel, 2015). The orbits are integrated in the plane of a two-body system with test particles begun in circular orbits but at different initial orbital semi-major axes. One massive particle is a moon and it orbits the other massive particle, the planet, in a circular orbit. The orbits were integrated with a moon-to-planet mass ratio $\mu = 10^{-11}$ similar to that of Pan. However, the morphology of these orbits in units of the Hill radius is not strongly dependent on the mass ratio, as long as μ is small. We verified this insensitivity by making the same plots for mass ratio $\mu = 10^{-7}$. The initial conditions for the test particles were computed from orbital elements using Jacobi or center of mass coordinates. The test particles were initially thousands of Hill radii away from the moon.

Test particle orbits in the frame rotating with the moon are shown in both panels of Figure 2. Orbits were begun at orbital semi-major axes both inside and outside the moon's orbit. The axes show distances in units of the moon's Hill radius, $R_H = a(\mu/3)^{\frac{1}{3}}$, with origin at the location of the moon's center. Here a is the moon's orbital semi-major axis. Figure 2a shows a larger region than Figure 2b. In Figure 2b we show test particle velocities subtracted by the moon's orbital velocity as vectors. Both positions and velocity vectors have been rotated so that the moon-planet line lies along the y-axis. The planet is found below, on the negative y-axis and the leading side of the moon is to the left. The central position of the moon is shown with a black dot on both panels in Figure 2. With grey dotted lines we show effective potential contours

$$V_{\text{eff}} = -\frac{r_{cm}^2}{2a^2} - \frac{(1-\mu)}{r_p/a} - \frac{\mu}{r_m/a}, \qquad (7)$$

where r_{cm} is the radius from the center of mass of the two-body system, r_p is the radius from the planet, and r_m is the radius from the moon. The effective gravitational potential for the restricted 3-body problem is computed in the rotating frame, with angular rotation rate that is in units of the mean motion n of the moon. The saddle
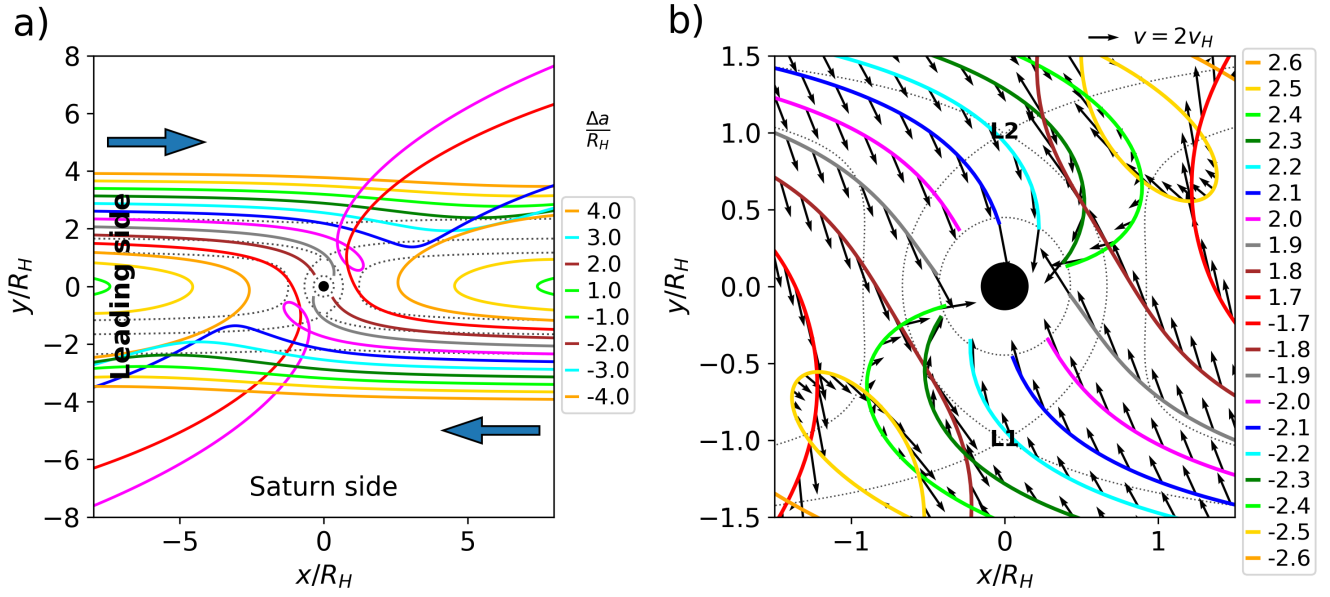
Figure 2: Test particle orbits in the frame rotating with a moon that is in a circular orbit about a planet. The moon's center of mass is shown with a black dot in the center of each plot. The x and y axes are in units of the Hill radius and the moon is centered at the origin. The planet is located on the negative y axis. The leading side of the moon is on the left. Test particles were begun at zero eccentricity and inclination and at different orbital semi-major axes in orbit about the central planet. The orbits were computed with satellite-to-planet mass ratio $\mu = 10^{-11}$, however, the morphology of these orbits in units of R_H is not dependent on the mass ratio μ as long as this ratio is low. Each test particle orbit is shown with a different color line and is labelled in the key by its initial semi-major axis in units of R_H from that of the moon's orbit. Grey dotted contours show levels of the effective potential, V_{eff} (see equation 7). The saddle points of the effective potential are the L1 and L2 Lagrange points, with L1 on the bottom side which faces the planet. a) We show the test particle orbits. Thick blue arrows show the initial direction of motion of the orbits in the rotating frame. b) Similar to a) except showing the region closer to the moon and velocity vectors. Velocity vectors are differences between the instantaneous velocity of the orbiting particle and the moon. A vector on the upper right shows a velocity with magnitude twice the Hill velocity v_H. Test particle impact sites onto the moon depend on their initial semi-major axis and how much of the Hill sphere is filled by the moon. We find that test particles on initially planar circular orbits can impact the moon at almost any location on the moon's equator.
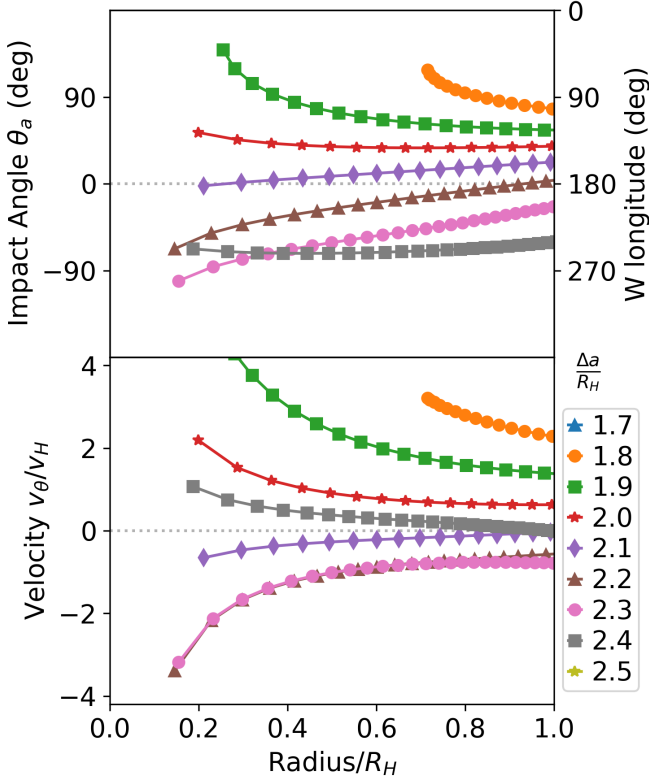
Figure 3: Angle and tangential velocity of test particle trajectories. The top panel shows impact angle, measured from the moon/planet line ($+y$ axis), as a function of radius from the moon center for test particle orbits shown in Figure 2b. This angle determines the impact longitude (on the moon's equator) of accreting material (see Figure 4 for an illustration of this angle). The bottom panel shows the tangential velocity component for the same orbits as a function of radius from the moon and is in units of the Hill velocity v_H. The tangential velocity component times the radius gives the spin angular momentum of accreting material. Accreted material with a positive value of v_θ would spin up the moon. The key shows the different offsets Δa between initial test particle orbit semi-major axis and that of the moon in units of the Hill radius R_H. We only show particles originating in orbits exterior to the moon's orbit. Particles originated interior to the moon's orbit would have impact angles rotated by 180° from that at the same $|\Delta a|$ but originating exterior to the moon's orbit. Test particles that did not come within a Hill radius of the moon on their first approach are not plotted.
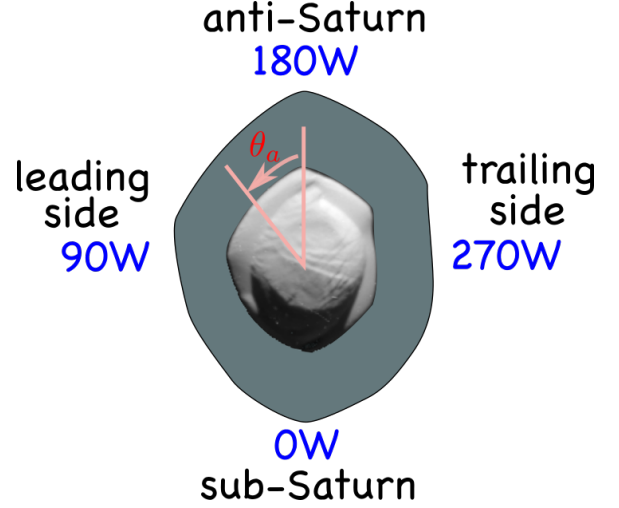

Figure 4: Our impact or accretion angle θ_a with a grey silhouette by Thomas and Helfenstein (2020) of Pan's equatorial ridge as seen from above its North pole and looking downward onto Pan. We also mark conventionally used planetocentric West longitudes. Inside the silhouette is the image N1867602962 of Pan which was observed at a ring elevation of 71°.

points of the effective potential are the L1 and L2 Lagrange points at about 1 Hill radius from the moon, with L1 on the side of the moon facing the planet.

Each test particle orbit in Figure 2 is plotted with a different color line and the lines are labelled in the keys by the difference between their initial orbital semi-major axis and that of the moon. This offset, Δa, is labelled in units of Hill radius, R_H. The test particle orbit shapes in Figure 2 are consistent with the orbits of ring particles initially in circular orbits that are integrated using Hill's equations (Dermott and Murray, 1981; Hedman et al., 2013).

Charnoz et al. (2007) proposed that accreting ring material would primarily flow through the L1 and L2 Lagrange points, at a distance of about 1 Hill radius away from the moon center and above and below the moon in Figure 2. This implies that accreting material from ring material inside Pan's orbit would primarily impact Pan on the Saturn side after going through the L1 Lagrange point, and the opposite would be true for accreting material entering from outside Pan's orbit and entering through the L2 Lagrange point. The numerical simulations by Charnoz et al. (2007) confirmed this expectation as they showed that impacts on Pan and Atlas occur preferentially near sub- and anti-Saturn points on the moon's equator. In contrast, our Figure 2 shows the impact locations could be almost anywhere on the moon's equator and the impact point depends on the initial orbital radius of the test particle. If the accreting material comes from the edge of a cold ring, with low velocity eccentricity dispersion, then the impact longitude on the moon is dependent upon the distance of the ring edge from the moon's orbit.

Figure 2 shows that only particles with initial conditions restricted to a range of initial semi-major axes, or Δa, would impact the moon. Test particles with small ini-

tial offset $|\Delta a|/R_H \lesssim 1.7$ have orbits initially similar to horseshoe orbits. They don't impact the moon on their first close approach to the moon. If the orbit integrations were carried out for longer periods of time, some might impact the moon (Dermott and Murray, 1981). Our test particles are initially in circular orbits to mimic the role of collisions in the ring. In high-opacity rings, collisions swiftly reduce particle eccentricity to a level lower than 10^{-8} (Rein and Papaloizou, 2010).

Particles in initially circular orbits which can impact the moon upon first approach are restricted to a small range in initial orbital semi-major axis, $1.7 \lesssim |\Delta a|/R_H \lesssim 2.5$, confirming similar numerical results by Karjalainen (2007) (see their Figure 1). Within this range, test particles initially external to the moon and at larger semi-major axis impact the moon on the trailing side, whereas those at lower Δa impact the moon on the leading side, as expected (Charnoz et al., 2007). Orbit trajectories initially within the moon's orbit are similar to those initially outside the orbit after rotation by 180°.

In Figure 3's top panel, we record test particle trajectory impact angles and in Figure 3's bottom panel we show tangential velocity components as a function of radius from the moon center in units of Hill radius. The longitude of an impact depends on the radius of the moon surface or how much of the Hill sphere is filled by the moon itself. The impact angle is counter-clockwise from the positive y axis on Figure 2 and increases in the same direction as the orbit's true anomaly. To make the convention for this angle clear, in Figure 4 we show our impact or accretion angle θ_a with a labelled silhouette (based on Figure 5 by Thomas and Helfenstein 2020) of Pan's equatorial ridge as seen from the north. W longitude in degrees is labelled in Figure 4 and on the right axis in the top panel of Figure 3. With convention of zero longitude on the moon's sub-Saturn side, an impact angle of 0 corresponds to a longitude of 180° W. Western longitude on the moon increases in the clockwise and opposite direction as our impact angle. Figure 3 only shows particles originating exterior to the moon's orbit. Particles originating from inside the moon's orbit exhibit similar phenomena, except the impact angle should be shifted by 180°.

The tangential velocity component in the bottom panel of Figure 3 is shown in units of Hill velocity, $v_H \equiv R_H n$ where n is the mean motion of the moon. Hill velocities in m/s are listed for the three moons in Table 2. The tangential velocity component is computed from the velocity difference between test particle and moon center and uses the moon center as origin to specify radial and tangential directions. The tangential velocity component times the radius gives the spin angular momentum per unit mass of accreting material that impacts the moon. Figure 3's bottom panel shows that the angular momentum per unit mass of accreting material is of order the Hill velocity times the Hill radius, $v_H R_H$. This size-scale is consistent with the estimate for the torque due to accretion we made in section 2.2 (Equation 4). The specific value of spin an-

gular momentum depends on the initial test particle orbit semi-major axis and at a lesser sensitivity, the location of the moon surface. In tidal lock, the spin angular rotation rate of the moon on our plots is counter-clockwise. Trajectories at larger initial semi-major axis offset $|\Delta a|$ have negative tangential velocity component v_θ and in the absence of tidal alignment, the accretion stream would slow the moon's rotation. The opposite is true for the test particles with smaller values of $|\Delta a|$ and these would increase the moon's spin rate.

In summary, integration of initially circular orbits on first close approach shows that only particles with orbital semi-major axes satisfying $1.7 \lesssim |\Delta a|/R_H \lesssim 2.5$ are likely to impact a moon. We confirm the range found previously through numerical integration (Karjalainen, 2007) (see their Figure 1). Particles can impact the moon's surface at almost any longitude on the moon's equator. The impact longitude and angular momentum per unit mass of accreting material depend on particle orbit semi-major axis and at a lower sensitivity on the radius of the moon's surface within the Hill sphere.

4.1. Accretion while tidally locked and in a circular orbit

We consider a moon core, in a circular orbit, that is accreting at a rate $\dot{M} < \dot{M}_{cr}$ so the body remains tidally locked. We assume that the moon accretes via a narrow accretion stream that hits the moon at a particular impact angle, θ_a, on the moon surface. If this angle differs from the principal body axes, then as mass piles up on the moon surface, the orientation of the principal body axes, with respect to the core, will vary. The moon would tidally realign so that its long principal body axis remains on the moon/planet line.

Our accretion or impact angle is zero, $\theta_a = 0$, when accretion flows directly through the L2 Lagrange point onto the moon and downward on Figure 2. This accretion angle increases in the counter-clockwise direction, since it is essentially the same thing as the impact angle discussed above (see Figure 4).

To explore numerically how accretion causes shape and body alignment changes, we mark a two-dimensional density array with ones and zeros depending upon whether mass is present in the pixel or not. The array pixels record density at locations in a Cartesian coordinate system for a two-dimensional body in the equatorial plane. The ones correspond to a uniform density material and zeros are empty space outside both core and accreted material.

The moon core is initialized by filling an oval region in the center of the density array with ones. The orientation of the body (and our density array) in the frame rotating with the moon's orbit is given with an orientation angle ϕ. Mass is consecutively added to the body surface along the impact angle θ_a to individual pixels in the array on the body surface. Mass is accreted by choosing a pixel that contains a zero value and changing it to one. We create a cost function for each pixel that increases as a function of angle from θ_a and with radius. The unfilled empty pixel
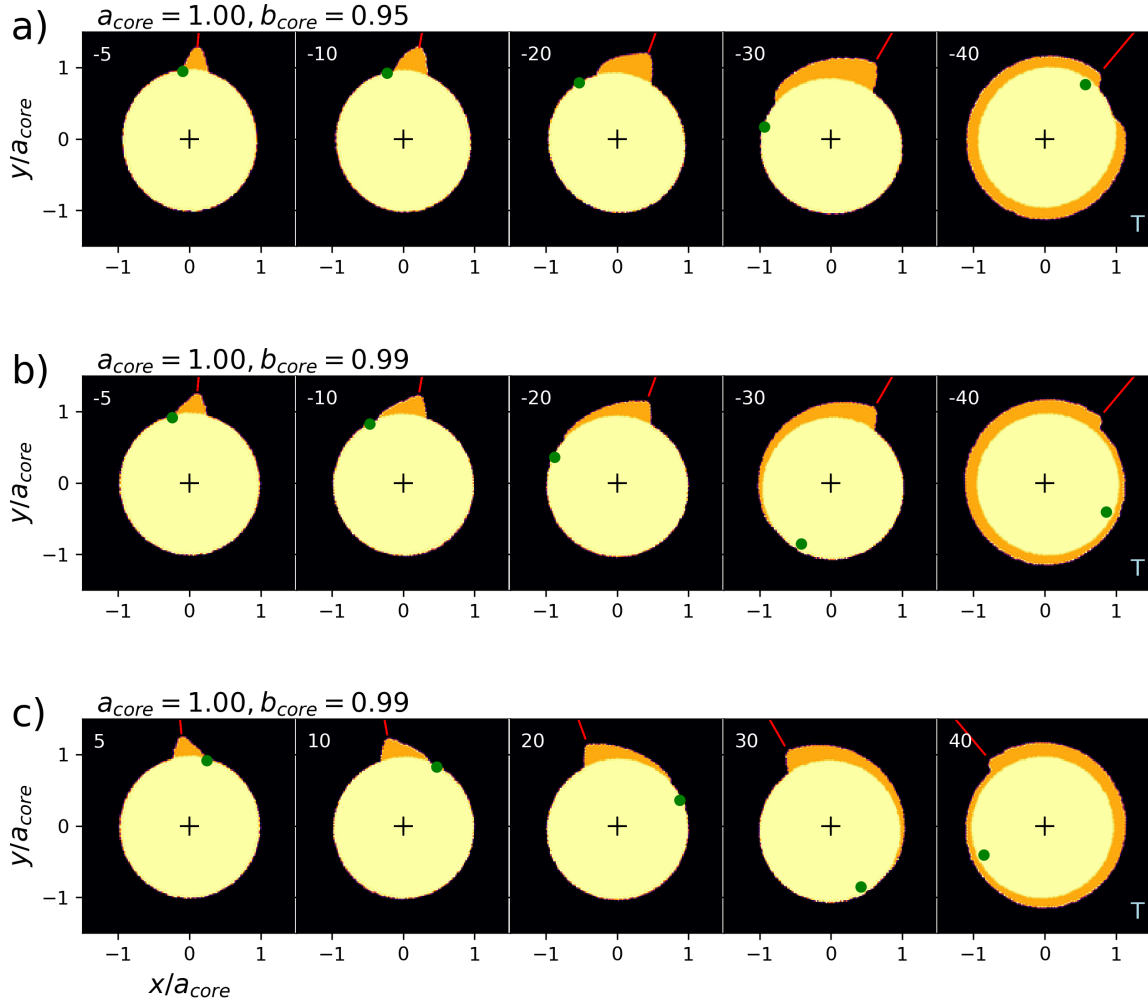
Figure 5: The distribution of accreted mass for a tidally locked moon. Each panel shows accretion at a different accretion angle θ_a with this angle in degrees labelled on the top left corner of each panel. The accretion stream is shown with a red line segment pointing to the impact point. A 'T' on the lower right of each row, signifies that the body remains tidally locked during accretion. However variations in body shape cause the moon to tilt slowly. The initial top side of the moon is labelled with a green dot. The tidal field is oriented so the moon's largest principal body axis remains aligned along the vertical direction. The moon's core is shown in yellow. The accreted material is shown in orange. The center of mass is shown with a plus sign. The axes are in units of the initial body semi-major axis which is initially oriented upward. These accretion simulations were done in 2 dimensions. a) The core's initial semi-axes are $a_{core} = 1.00$ and $b_{core} = 0.95$ and the accretion angles are negative. The slopes (derivative of radius w.r.t. longitude) of the lobes on Pan's equatorial ridge appear consistent with this sign. b) The core's initial semi-major and minor axes are 1.00 and 0.99 and the accretion angles are negative. The angular shift in body orientation is higher than in a) due to the core's rounder shape. c) The core's initial semi-axes are 1.00 and 0.99 and the accretion angles are positive.

9

with the minimum cost function is chosen during each mass accretion event. The cost function we used is the product of an exponential function of radius and an exponential function of distance from the line at angle θ_a that begins at the origin.

After a single pixel is filled, we recompute the center of mass position and the orientation of the body principal axes. Our procedure for computing the orientation of the long principal body axis is described in Appendix A. We rotate the body about its center of mass by updating ϕ so that the body's longest principal axis remains aligned vertically. This rotation maintains tidal alignment. We recompute the center of mass and ϕ for each parcel of mass that is added to the body. Figures or rows of figures where tidal alignment is maintained during accretion are marked a blue 'T' in one of the corners of the figure.

We illustrate body shapes and orientations arising from accretion along 5 different accretion angles in Figure 5. The axes are shown in units of the moon's initial core semi-major axis. The initial core is shown in yellow and the accreted material is shown in orange. A green dot shows a position on the core that was initially oriented on the anti-planet side (upward as in our previous figures). Each panel in Figure 5 shows accretion at a different angle θ_a that is labelled in degrees on the top left side of the panel. The angle of accretion is marked with a short red segment outside the body.

For small values of impact angle θ_a, accreted mass continues to pile up near the impact point. The accreted mass increases the longer principal body axis. The more mass that is added, the less the orientation angle of the core varies. This trend is illustrated with a simple model in Appendix A (see equation A.7). This gives a triangular wedge shape to the accreted material. The wedge shape resembles the shape of a single lobe of Pan's equatorial ridge. If $|\theta_a| \gtrsim \pi/4$ then the accreted mass tends to increase the mass distribution along the smaller principal body axis of the body (see equation A.10). The body becomes rounder and the angular shift caused by accretion is increased (equation A.7). The body continues to rotate, accumulating mass evenly around its equatorial ridge.

The lobes on Pan's equatorial ridge seem to increase in thickness and radial extent as the western longitude (on the equator) increases (see Figure 1), though this trend is not evident in the thinnest and most extended part of the ridge and from the silhouette shown in Figure 4. We can characterize Pan's lobes with a slope that is the derivative of their radial extent with respect to longitude. The wedges in our accretion model with accretion angle $\theta_a < 0$, as shown in Figure 5a, b. have the same slope as the lobes of Pan. The wedges have the opposite slope if the accretion angle $\theta_a > 0$, as shown in Figure 5c.

The rate the body core orientation angle changes while accreting depends on both core shape and on the accretion angle. If the core is elongated then more mass must be accreted to cause the same degree of rotation during accretion. This is illustrated with a comparison between
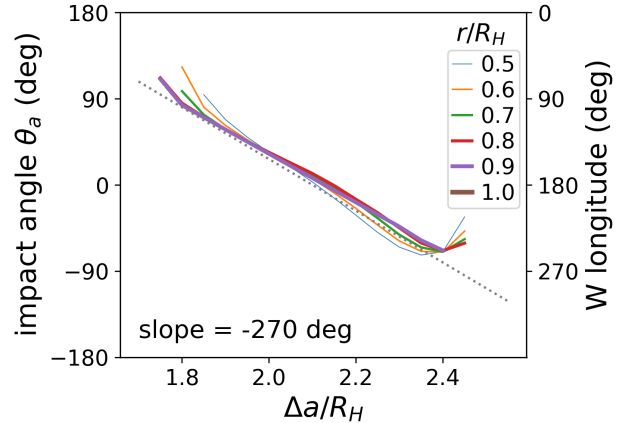

Figure 6: Impact or accretion angle θ_a in degrees as a function of initial test particle orbital semi-major axis distance from that of the moon $\Delta a/R_H$. These are computed from the same initially circular orbits external to a moon in a circular orbit that are shown in Figure 2. We have plotted the impact angle at five different surface radii from the moon center. The different lines represent the different surface radii and they are given in the key in units of the Hill radius R_H. The impact angle is only weakly dependent on the radius of the surface but is strongly dependent on the test particle's initial orbital semi-major axis. The grey dotted line is given in equation 8.

Figure 5a, and b. The initial cores in Figures 5b,c have semi-axis lengths 1.00 and 0.99 whereas those in 5a are initially more elongated with semi-axis lengths 1.00 and 0.95.

The simple accretion model explored here gives two types of morphology for material accreted on an equatorial ridge, single wedges or uniform accretion covering the entire equator. If accreting material came from both inside and outside the moon's orbit, the accreted material would be symmetrically distributed, with material coming from the planet side shifted by 180° from that accreted from the anti-planet side. The model does not give polygon-shaped equatorial ridges, like Pan, or ridges with a depression on one side of the moon, like Atlas. Because accretion has been restricted to the plane we also do not see ridges at different latitudes like those on Daphnis.

In summary, a tidal accretion model that takes into account body shape changes while maintaining tidal alignment and at a single accretion angle can give wedge-shaped or sloped lobes along an equatorial ridge if the accretion angle is low with respect to the moon/planet line. However, the model only illustrates single wedges or uniform accretion covering the entire equator. More complex models are required to match the morphology of Pan, Atlas or Daphnis.

4.2. Accretion from a gap edge

Up to this point we have considered accretion from material from a narrow ring of disk material that has a single orbital semi-major axis and giving an accretion stream that is confined to a single impact angle. Gravitational encounters with the moon usually push ring mate-
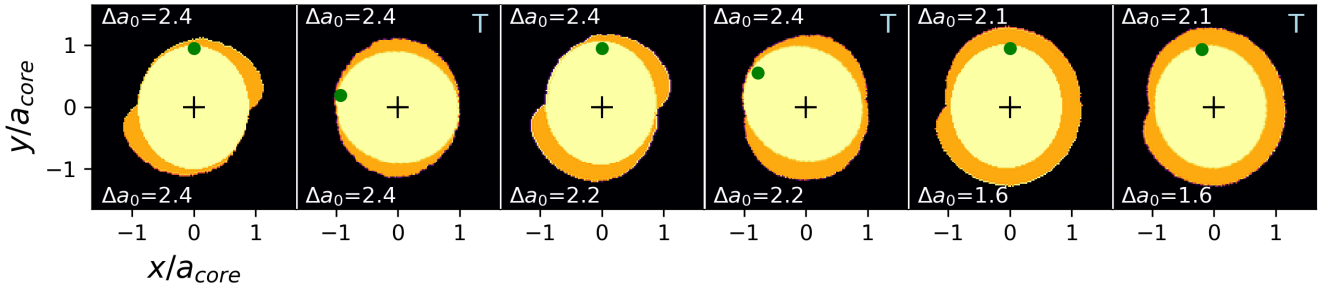
Figure 7: The distribution of accreted mass on a moon's equatorial ridge where accreted material originates from the outer and inner gap edges with mass surface density profiles that are described with equation 9. This figure is similar to Figure 5 except accreted material originates from a range of orbital semi-major axes and impact angles. The outer gap edge has edge location Δa_0 in units of R_H labelled on the top of each panel and the inner edge has Δa_0 in units of R_H labelled on the bottom of each panel. Only the panels labelled 'T' on the top right remain tidally locked during accretion. The others do not allow the body to rotate. The accreted material is shown in orange and the core is shown in yellow. The center of mass is shown with a plus sign. The plot axes are in units of the initial body semi-major axis of the moon which is initially oriented vertically. The core's initial body semi-axes are $a_{core} = 1.00$ and $b_{core} = 0.90$.

rial away from the moon (Goldreich and Tremaine, 1982; Weiss et al., 2009). The gap widens until torques driven by spiral density waves balance those associated with viscous spreading (Borderies et al., 1982, 1989; Lissauer et al., 1981; Goldreich and Tremaine, 1982; Porco et al., 2005; Tajeddine et al., 2017b). Right now the Keeler gap hosting Daphnis and the Encke gap hosting Pan are sufficiently wide that there is little or no accretion onto these moons. However, the gaps might have been narrower at some time in the past, allowing accretion. Models taking into account spiral density wave driven torque and diffusion in the gap edge have predicted gap edge surface density profiles (Grätz et al., 2019). The gap edge could display small scale structures, such as the few hundred meter length wispy features near the Keeler gap edge (Porco et al., 2005; Tajeddine et al., 2017b). In both settings, the surface density profile (averaged over ring longitude if wisps are present) drops significantly over a distance d_{edge} that is of order a Hill radius.

If the region allowing accretion overlaps the region where the surface density profile drops, then we expect more mass is accreted from impact angles arising from the denser and more distant regions of the disk. To illustrate the dependence of impact angle on initial semi-major axis we plot in Figure 6 the impact angle at 5 different radii from the body center as a function of initial orbital semi-major axis offset Δa from that of the moon. We have only plotted initially external orbits, with $\Delta a > 0$, using the same orbits as shown in Figure 2. The impact angle is weakly dependent on the radius of the surface but is strongly dependent on the test particle's initial orbital semi-major axis. The impact angle is approximately linearly dependent on initial test particle orbital semi-major axis offset Δa and is reasonably well described by

$$\theta_a(\Delta a) \approx -270° \left(\frac{\Delta a}{R_H} - 2.1 \right). \qquad (8)$$

We show this relation as a dotted grey line on Figure 6.

What slope in a gap edge would give lobes similar to those present on Pan's equatorial ridge? If the lobes vary by a factor of 2 in their linear mass density (mass per unit distance along the equator) across 90° in equatorial longitude, then the slope of equation 8 gives a distance $d_{edge} \sim 0.3R_H$ over which the surface density drops. This distance seems reasonable compared to analytical models of gap density profiles (Grätz et al., 2019).

Figure 7 illustrates some possible equatorial ridge morphologies that take into account the mass surface density profile in both inner and outer edges. We start with a surface density profile $\Sigma(\Delta a)$ describing edges with a Gaussian form

$$\Sigma(\Delta a) = \begin{cases} \exp\left(-\frac{(|\Delta a| - \Delta a_0)^2}{2R_H^2 \sigma_h^2} \right) & \text{if } |\Delta a| < \Delta a_0 \\ 1 & \text{otherwise} \end{cases} \qquad (9)$$

where Δa_0 describes the edge location and σ_h is a dispersion that determines how fast the profile drops near Δa_0. For equally separated values of Δa, we add mass particles onto our density array (as described in section 4.1) at impact angle that is computed using Equation 8 and is sensitive to Δa. Mass particles are added onto the body's surface with probability set by $\Sigma(\Delta a)$.

Equation 8 is used to relate Δa to the impact angle and determines where mass is added to the modeled equatorial ridge. Only mass originating between $1.7 < |\Delta a/R_H| < 2.4$ is allowed to accrete onto the body, as impacts don't occur outside this range. We simultaneously accrete from both outer and inner edges of a gap but we need not have the same edge location or gap profile dispersions in both edges. As described in section 4.1, the body can be continually reoriented while it is accreting so as to remain as if it were tidally locked throughout accretion.

Figure 7 shows 6 different equatorial ridge morphologies computed with gap profile dispersion $\sigma_h = 0.2$ and for different values of edge locations Δa_0 for inner and outer edges. The panels are in pairs, with tidally locked

11

accretion models to the right of a similar model with body rotation held fixed during accretion. The specific values for Δa_0 for the outer gap edge are written on the top of each panel and on the bottom of each panel for the inner gap edge. A gap profile gives higher mass density at larger $|\Delta a|$. Along with Figure 6, this implies that the linear mass density of an accreted lobe would increase with increasing western longitude (corresponding to more negative impact angle θ_a). This trend is evident in Figure 7 for most of the modeled accreted lobes and the mass per unit longitude of Pan's wedge-shaped lobes seem to increase in this direction.

If the gap profile remains constant during the accretion era, then accretion from the edge of a gap while in a circular orbit would allow growth of a single wedge-shaped lobe. If the moon simultaneously accretes from both outer and inner gap edges then two wedge-shaped lobes would accrete onto an equatorial ridge. If the outer gap edge is further away from the moon than the inner gap edge (the two rightmost panels in Figure 7) then less mass is accreted on the moon's leading side. An alternative explanation for the divot on the leading side of Atlas's ridge might be a difference in inner and outer gap edge surface density profiles. While Figure 7 illustrates a variety of equatorial ridge shapes, we don't see an equatorial ridge with multiple peaks or lobes like Pan's.

In summary, when accreting material is originally in a circular orbit and impacts a moon in a circular orbit, there is a nearly linear relation between the initial semi-major axis offset Δa of the accreting material from the moon, and the impact angle on the moon's equator. A moon accreting from an outer gap edge would accrete more mass at larger western longitude on its equator. The slope of an accreted wedge would be related to the slope of the surface density profile in the gap edge. If the outer gap edge is further away from the moon than the inner gap edge then less mass is accreted on the moon's leading side, giving a possible alternative explanation for structure on Atlas's equatorial ridge. However, accretion onto a moon in a circular orbit from inner and outer gap edges does not seem to give an equatorial ridge with multiple peaks or lobes like Pan's.

4.3. Accretion onto a moon on an inclined orbit

Charnoz et al. (2007) suggested that the thickness of the equatorial ridge of Pan and Atlas might be related to their orbital inclinations. We examine impact locations for test particles initially in circular orbits that impact a moon that is on an inclined orbit with respect to the plane containing the test particles. During the encounter, test particle trajectories are sensitive to the height of the moon, in its orbit, above or below the plane containing the test particles (the ring plane). The Hill inclination $i_H \equiv \frac{R_H}{a}$ is the inclination required for the moon to travel a Hill radius R_H above the ring plane or equivalently Saturn's equatorial plane. At large inclination ($i > i_H$), impact with the moon is less likely because the distance between
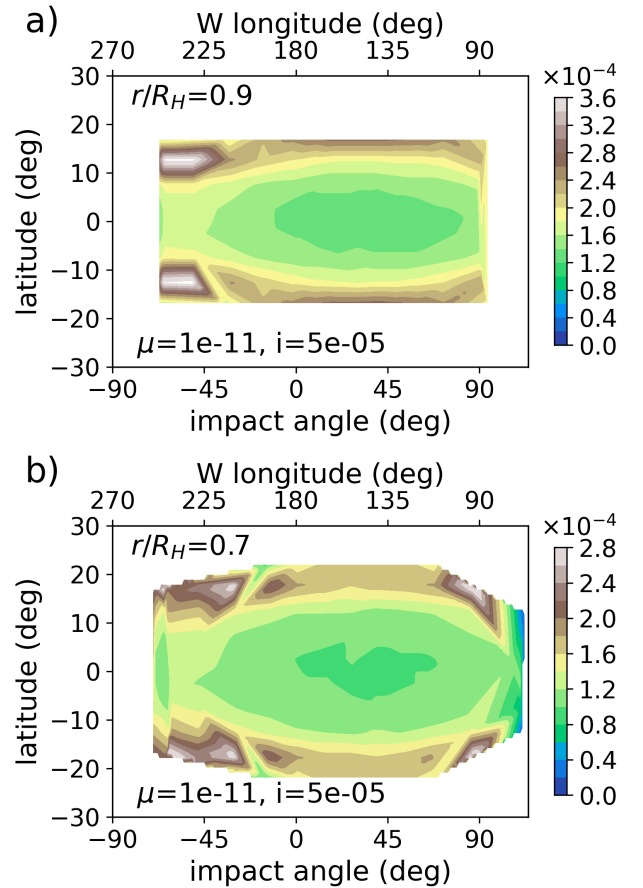

Figure 8: Distribution of impact latitude and longitude on a moon by test particles initially in zero inclination and circular orbits, external to a moon's orbit, that impact a moon on an inclined orbit. The bottom axes shows our impact angle θ_a in degrees and the top axes shows W longitude. The vertical axis is latitude in degrees. The moon has mass ratio $\mu = 10^{-11}$ and orbital inclination $i = 5 \times 10^{-5} \approx 0.3 i_H$. The colour map shows the fraction of test particles per square degree that impacted at a particular location. a) Impacts are recorded at $r = 0.9 R_H$ from the moon center of mass. b) Impacts are recorded at $r = 0.7 R_H$ from the moon center of mass.

particle and moon orbits can be larger than if both were in the same plane. Particles that impact the moon can impact over a wide range of possible latitudes on the moon. Because the equatorial ridges of Pan, Daphnis and Atlas are thin, their orbital inclinations probably remained low during accretion of their equatorial ridges (Charnoz et al., 2007), with $i < i_H$. To explore this regime, we carried out test particle integrations for a moon with mass ratio $\mu = 10^{-11}$ and with orbital inclination $i = 5 \times 10^{-5}$ which is $\approx 0.3 i_H$. For comparison, the inclination of Pan is probably less than its Hill inclination (within errors), whereas Daphnis' current inclination is 100 times its Hill inclination and Atlas' inclination is 20 times its Hill inclination. Due to its orbital inclination, Daphnis excites vertical waves on the edges of the Keeler gap (Weiss et al., 2009).

Test particle trajectories near the moon depend on their initial orbital true longitude because upon close approach, the moon can be at different heights above or below the ring plane. We integrated $N_{\text{test}} = 400$ test particle orbits for each initial test particle semi-major axis, Δa, but each particle in the set is initially at a different orbital longitude. The separation in orbital longitude between consecutive initial test particles is $\frac{2\pi \Delta n}{N_{\text{test}}}$ where $\Delta n = n' - n \approx n \frac{3}{2} \frac{\Delta a}{a}$ is the difference between test particle and moon mean motions. This separation ensures that we sample the entire range of possible close encounter behaviors.

Figure 8 shows the distribution of impact locations, computed from orbits with initial semi-major axes $\Delta a/R_H \in$ 1.75 to 2.5 with a spacing of 0.05. The impact angle or W longitude is set by the initial orbit semi-major axis Δa. At a particular Δa, since the inclination is low, the test particle impact angle is within a few degrees of that computed when the moon orbital inclination is zero (see Figure 6). Figure 8a shows impact surface density maps for orbits that impact a spherical surface at a radius $r = 0.9 R_H$ from the moon center. Figure 8b is similar except at $r = 0.7 R_H$. The latitude and longitude distributions are wider at the smaller surface radius due to the gravitational acceleration of the moon itself. This is consistent with the higher impact velocities seen in the lower panel of Figure 3.

Figure 8 shows that fewer impacts hit near the equator than at latitudes of 10–20°. The higher latitude impacts are test particles deflected vertically when the moon was cresting above or below the ring plane. We confirm the peaked impact latitude distribution shown in the simulations by Charnoz et al. (2007).

Pan's and Atlas' equatorial ridges are not U-shaped. They don't have a divot on their equator and bulges above and below the equator, as would be suggested by Figure 8 and Figure 2A by Charnoz et al. (2007). We have not explored scattering or rolling on the surface after impact or inter-particle collisions during accretion. Latitude distribution would also be sensitive to orbital eccentricity. Models that include additional processes are probably needed to explain the thickness distribution of Pan's equatorial ridge. However, some of the fine features present on these ridges are likely to be related to the orbital inclination of the moon during accretion and the inclination of the particles that were accreted.

In summary, we have examined the latitude distribution of impacts for accretion of a moon in a circular but inclined orbit by ring material that is initially in a circular orbit. As was true for coplanar moon and particle circular orbits, the longitude of impact is dependent on the initial test particle semi-major axis. At low inclination, $i \lesssim i_H$, test particle impact angle is similar to the impact angle when the moon and test particle orbits are coplanar. We integrated impacting test particle orbits for a moon with mass ratio $\mu = 10^{-11}$ and orbital inclination $i = 5 \times 10^{-5} \approx 0.3 i_H$ and found that the latitude distribution of impacts is U-shaped, confirming the simulations by Charnoz et al. (2007), with more particles impacting at latitudes of 10–20° than on the equator. This implies that orbital eccentricity or additional processes, such as scattering on the surface, collisions in the accretion stream, or mass redistribution are required to account for ridge thickness and latitude distribution.

5. Test particles that impact a moon in an eccentric orbit

Charnoz et al. (2007) showed that the longitude distribution of accreting ring material onto a moon depends upon the moon's orbital eccentricity. In this section, we look at impact angles for test particles, initially on circular orbits, that approach a moon that is on an eccentric orbit. For a moon on a circular orbit, the morphology of the approaching test particle orbits in units of the Hill radius is not strongly dependent on moon-to-planet mass ratio, μ. However if the moon is on an eccentric orbit, then an additional spacial scale enters the problem, the radial distance travelled between pericenter and apocenter. If the radial distance travelled in the orbit is less than a Hill radius, the impacting orbits should be similar to those impacting a moon in a circular orbit. The Hill eccentricity

$$e_H \equiv \frac{R_H}{a} \qquad (10)$$

is the orbital eccentricity required for the moon to travel $2R_H$ radially between orbit pericenter and apocenter. If the orbital eccentricity $e \ll e_H$, we expect the impacting orbits would be similar to those discussed in section 4. We list the Hill eccentricities for Pan, Daphnis and Atlas in Table 2. Currently Pan's orbital eccentricity is below its Hill eccentricity, whereas Daphnis has an eccentricity similar to its Hill eccentricity and Atlas's eccentricity exceeds its Hill eccentricity.

The distance from the edges of the Encke gap to Pan in units of Pan's orbital semi-major axis are $\Delta a/a = 1.2 \times 10^{-3}$ and in units of Hill radius are $\Delta a/R_H = 8.45$. The distance from the edges of the Keeler gap to Daphnis in units of Daphnis's semi-major axis is $\Delta a/a = 1.5 \times 10^{-4}$
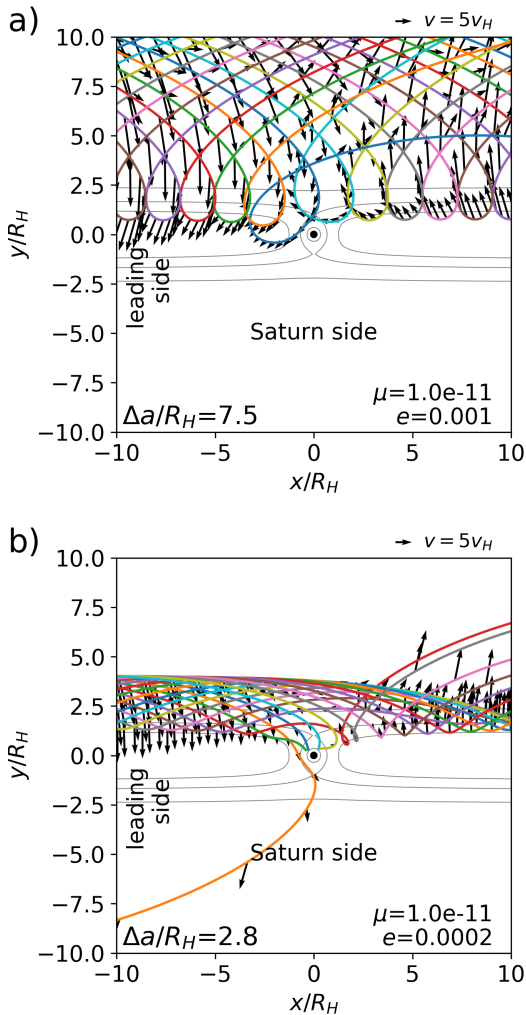
Figure 9: Test particle orbits near a moon in an eccentric orbit. These figures are similar to Figure 2 except the moon has an orbital eccentricity. The mass ratio $\mu = 10^{-11}$ is similar to that of Pan. The planet facing side of the moon is on the bottom and the leading side of the moon is on the left. Each orbit has the same initial orbital semi-major axis but begins at a different orbital true longitude. The orbits are shown in a frame that puts the moon center at the origin and the planet on the negative y axis. Black velocity vectors show the difference between test particle and moon velocity. The scale of these vectors is shown with an arrow on the upper right that has length 5 v_H where v_H is the Hill velocity $v_H = nR_H$. The test particles are initially on circular orbits outside the orbit of the moon with initial semi-major axis Δa shown on the bottom left of the plot. When the moon is at apocenter, the test particles are at the bottom of a loop. Because the angular rotation rate of the moon slows at apocenter, the test particles can approach the moon from the right, rather than the left. a) The moon's eccentricity is $e = 0.001 \approx 7e_H$. b) The moon's eccentricity is $e = 0.0002 \approx 1.4e_H$. The size of the loops depends on the moon's eccentricity and initial test particle orbit semi-major axis offset $\Delta a/R_H$.

and in units of Hill radius $\Delta a/R_H = 4.3$. The outer edge of the A-ring is at a semi-major axis of $a \sim 136,769$ km approximately at the location of the 7:6 inner Lindblad resonance with Janus (Porco et al., 1984; Spitale and Porco, 2009). The distance of Atlas from this edge is currently $\Delta a/a = 6.5 \times 10^{-3}$ or $\Delta a/R_H = 43$. As the distances to the ring edges in units of Hill radius are greater than 1, an eccentricity $e > e_H$ would be required for the moons to accrete ring material from gap edges. However, in the past, ring edges could have been at different distances from the moons and the moon eccentricities could have been higher.

To characterize the regime where moon orbital eccentricity exceeds the Hill eccentricity $e > e_H$, we examine impacting orbits for a moon with mass ratio $\mu = 10^{-11}$ similar to that of Pan, and with an orbital eccentricity large enough that Pan can graze the edge of the Encke gap, $e = 0.001 \approx 7.1e_H$. We also examine impacting orbits at a moon eccentricity of $e = 0.0002$ which is $\approx 1.4e_H$ in terms of Pan's Hill eccentricity and about 14 times Pan's current eccentricity. These integrations characterize the regime with eccentricity $e \sim e_H$. With a moon on an eccentric orbit, test particles are initially in circular orbits to mimic originating from a dense collisional ring edge. Test particle orbits for $e = 0.001$ and 0.0002 are shown in Figure 9 and at a smaller scale in Figure 10. Orbit positions have been rotated and shifted so that the moon remains at the origin and the planet remains along the negative y-axis.

Test particle trajectories near the moon depend on their initial orbital true longitude because upon close approach, the moon can be at different radii from the planet. As in the case of the inclined moon (section 4.3), we integrated $N_{\text{test}} = 400$ test particle orbits for each initial test particle semi-major axis, where each particle in the set is initially at a different longitude. The separation in orbital longitude between consecutive initial test particles is $\frac{2\pi \Delta n}{N_{\text{test}}}$ where $\Delta n = n' - n \approx n\frac{3}{2}\frac{\Delta a}{a}$ is the difference between test particle and moon mean motions. This separation ensures that we sample the entire range of possible close encounter behaviors. Only some of the integrated orbits are plotted in each Figure.

Figure 9a shows test particle orbits, begun at semi-major axis with $\Delta a/R_H = 7.5$, that experience a close encounter with the moon with $e = 0.001$ on their first close approach. Close encounters occur when the moon is near apocenter and at that time its angular rotation rate in the inertial frame slows. The test particles, which are begun in circular orbits, initially have constant angular rotation rates. In a moving and rotating frame that keeps the moon at the origin, the test particle orbits show loops. Impacts can come from the right, and hit on the moon's trailing side, rather than from the leading side of the moon, even though these external orbits were initially approaching the moon from the left and leading side and outside the moon's orbit. Charnoz et al. (2007) also noticed that particles originating from outside the moon's orbit impacted on the
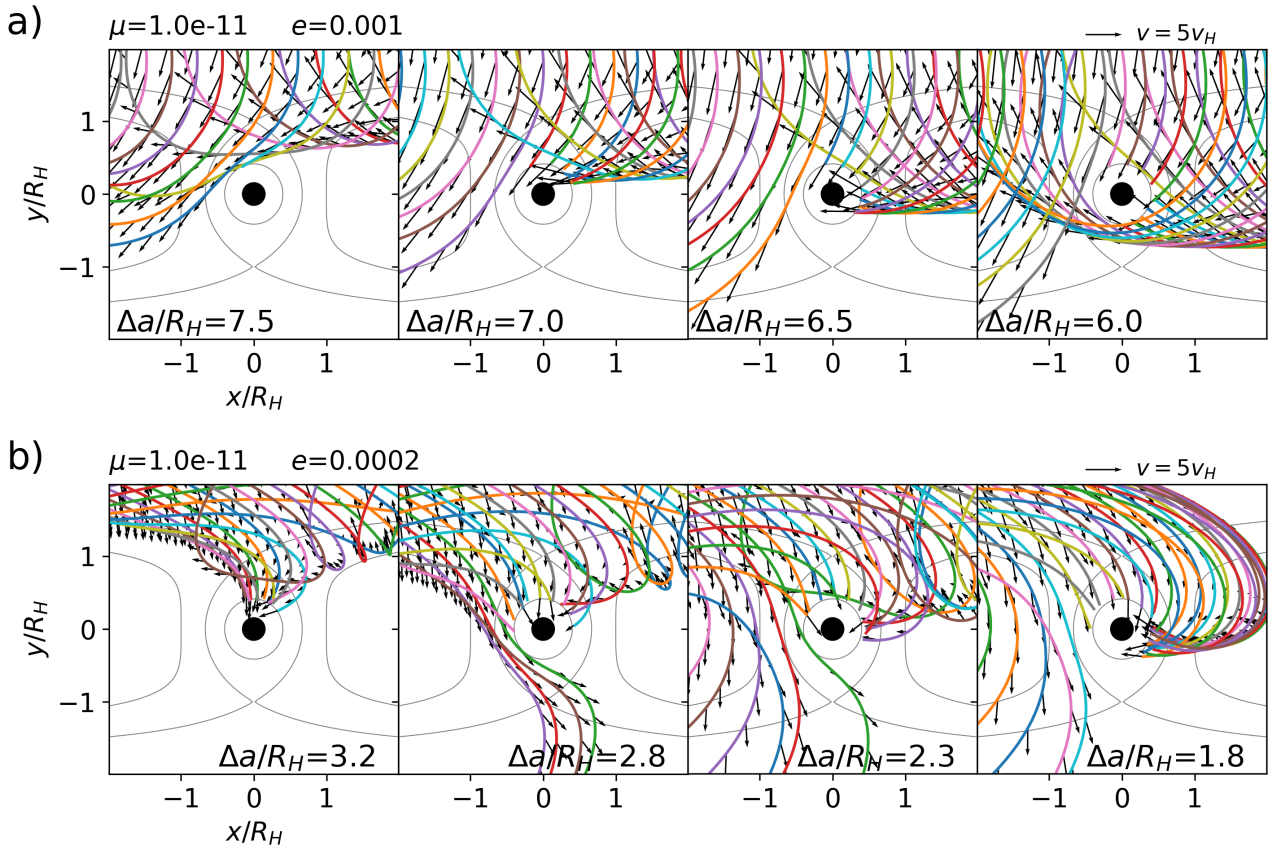
Figure 10: Test particle orbits near a moon of mass ratio $\mu = 10^{-11}$ and in an eccentric orbit. Each panel is similar to Figure 9 except the axes span a smaller range. Each panel shows a different initial semi-major axis for the test particle orbits, with $\Delta a/R_H$ labelled on the lower left of each panel. In each panel, the different test particle orbits are begun in circular orbits at different but evenly spaced orbital true longitudes. a) The moon has orbital eccentricity $e = 0.001 \approx 7.1e_H$. b) Similar to a) except $e = 0.0002 \approx 1.4e_H$ and with different values for the initial test orbit semi-major axis offsets $\Delta a/R_H$.

trailing side instead of the leading side in simulations of an eccentric Atlas. Figure 9b is similar except $\Delta a/R_H = 2.8$ and the moon's orbital eccentricity $e = 0.0002$. The loops are smaller in this case and one orbit passes from outside the moon to inside the moon's orbit. Encounters such as these can facilitate the moon's radial migration (e.g., Ida et al. 2000).

In Figure 10a we show test particles orbits begun at different initial semi-major axes, with $\Delta a/R_H = 7.5, 7.0, 6.5$ or 6.0, respectively for moon orbital eccentricity $e = 0.001$. Figure 10b shows orbits with $\Delta a/R_H = 3.2, 2.8, 2.3$ or 1.8 for orbital eccentricity $e = 0.0002$. Each panel shows test particle orbits with a single initial orbital semi-major axis. The offset Δa in units of the Hill radius is labelled at the bottom of each panel. Figure 10 shows that at each initial semi-major axis, impacting test particles have a range of impact longitudes on the moon, depending upon the position of the moon in its orbit during the encounter. We confirm the numerical results by Charnoz et al. (2007), modeling Atlas' equatorial ridge, finding that a moon on an eccentric orbit would probably accrete material covering a wider range of longitudes on its equator than a moon on a circular orbit.

In Figure 11 we show with blue-green lines the same orbits as in Figure 10 but plotted as a function of angle θ_a from vertical (the impact angle used in section 4 and shown in Figure 4). The impact angle is on the y-axis in degrees and radius from the moon center is on the x-axis in units of Hill radius. These figures show the orbit impact angle as a function of radius of the moon surface and also illustrate that for each initial orbital semi-major axis, impacting test particles have a range of impact longitudes on the moon's equator.

Figure 11 shows that smaller separation in orbital semi-major axis $|\Delta a|$ gives a lower mean impact angle. This is opposite to the trend seen for a moon in a circular orbit. Since orbits were begun evenly spaced in orbital longitude, their number density can be used to estimate the fraction of accreted mass that would impact the moon as a function of longitude on its equator. We resampled the integrated orbits at each moon radius to produce the colored images which show the number density of particles that would impact a moon as a function of impact angle (the y-axis) and for different possible moon radii (the x-axis). The number density has been normalized so that the total number density integrates to 1 at radius $r = R_H$. Because test particles are initially equally spaced in their circular orbits, we can compute the fraction of particles that impact the moon, assuming that they are initially evenly distributed over the entire circular orbit. The fraction of test particles f_a, that cross inside $r = R_H$ is recorded on the top left of each figure. In the integrations shown in Figure 11, test particles on orbits initially closer to the moon are more likely to accrete onto the moon. Equivalently, the accretion rate is higher for the lower values of offset $|\Delta a|$.

A comparison between Figures 10a and b and between Figures 11a and b shows that the trajectories at moon or-

bital eccentricity $e \gg e_H$ differ from those at $e \sim e_H$. For $e = 0.0002 \sim 1.4 e_H$, the test particle loops seen in the moon's frame of reference are smaller and this gives accretion on both leading and trailing sides, particularly at the larger values of $|\Delta a|$. Accretion tends to be stronger at most impact angles on the leading side for orbital eccentricity $e = 0.001 \sim 7.1 e_H$ and $\Delta a > 0$. At even smaller $|\Delta a|$ than shown in Figure 10 the most extreme point on orbit loop lies outside the Hill radius on the opposite side of the moon, so impacts are more evenly distributed in angle than those shown for $e = 0.001$.

As discussed in section 4, particles that impact the moon with positive tangential velocity component, $v_\theta > 0$, could increase the moon's rotation rate. In Figure 12 we compute the average tangential velocity component, v_θ, of the accretion stream, integrated over impact angle, and as a function of radius from the moon's center of mass. We show the average tangential velocity component for the different initial test particle semi-major axis and with orbits shown in Figure 10 and for the two different moon eccentricities. With the moon in a circular orbit, (see Figure 3b) and test particles originating from outside the moon's orbit, we found that impacting test particles have $v_\theta > 0$ for lower initial semi-major axis offset $|\Delta a|$. Here with the moon in an eccentric orbit, we see the opposite trend, $v_\theta > 0$ at larger $|\Delta a|$. This trend is seen because test particles tend to impact the moon at the bottom of a loop, as seen in the frame moving with the moon, and so coming from the trailing side (see Figure 9 showing the loops). The size of the tangential velocities is similar to the Hill velocity v_H, confirming our estimate for the critical accretion rate $\dot{M}_{cr}$ discussed in section 2.2.

5.1. Accretion onto a moon that is on an eccentric orbit

Thomas and Helfenstein (2020) have recently updated shape models for Pan and Atlas. Their new models include estimates for ridge-removed core axis ratios which we have listed in Table 1. In Figure 13 we show similar elongated cores that have accreted mass along their equators. The angular distributions of accreted mass are based on the distributions, shown in Figure 11, we constructed from test particle orbit integrations. In each panel in Figure 13, the core is shown in yellow and the accreted mass is in orange. The green dot shows a core position that was originally on the positive y axis prior to accretion. The cores have axis ratio $b_{core}/a_{core} = 0.83$ and semi-major axis $a_{core} \approx 0.8 R_H$ based on the ridge-removed model for the core of Pan (Thomas and Helfenstein, 2020). The accretion is done in two dimensions and as described in section 4.1. However, instead of allowing accretion at a single angle, we consecutively add mass to pixels in the mass density array using a probability that is equal to that found at equivalent angle and radius in the density distributions that we computed from the test particle orbits.

In Figure 13, the panels in each row show material accreted from test particle orbits at different initial orbital
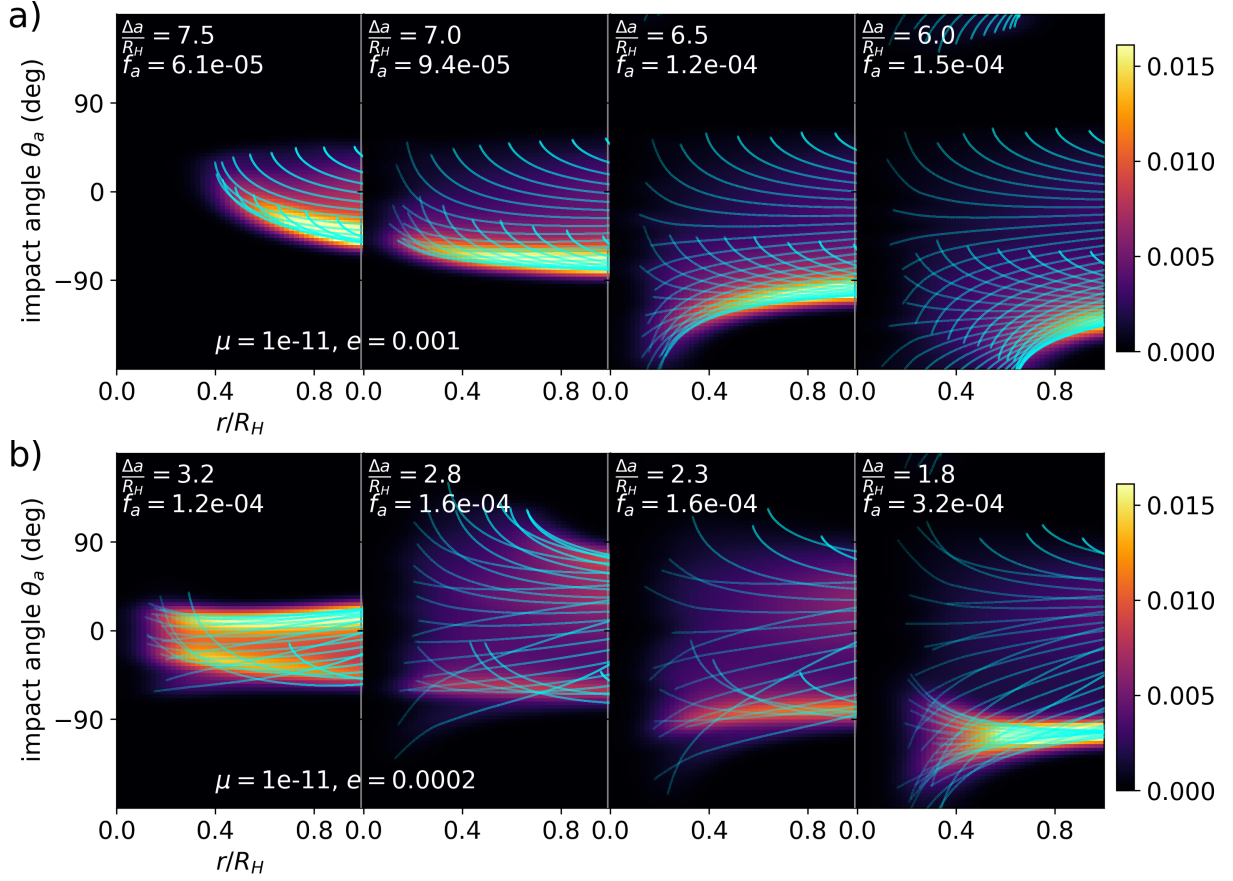
Figure 11: The impact angle distribution of material accreting onto a moon that is on an eccentric orbit. In each panel, blue-green lines show test particle orbits but as a function of impact angle (y-axis) and radius (x-axis) from the moon's center of mass. The y axis is in degrees and the x axis in units of the Hill radius. The color image shows where mass accumulates on the surface of an accreting moon. The colored density images are histograms constructed from the number of orbits that crossed each radius and impact angle. The distribution of accreted mass on the moon's equator as a function of the moon's longitude can be estimated by choosing a vertical slice in the density image with radius given by the moon's surface radius. The fraction of impacting test particles f_a is recorded on the top left of the panel. The colour-bar scales shows the fraction of particles that impact per degree in impact angle. This is normalized so the integral over impact angle of the distribution at $r = R_H$ is 1. The orbits are the same as shown in Figure 10 and are for a moon with mass ratio $\mu = 10^{-11}$. a) For moon orbital eccentricity $e = 0.001 \approx 7.1 e_H$. b) For moon orbital eccentricity $e = 0.0002 \approx 1.4 e_H$.
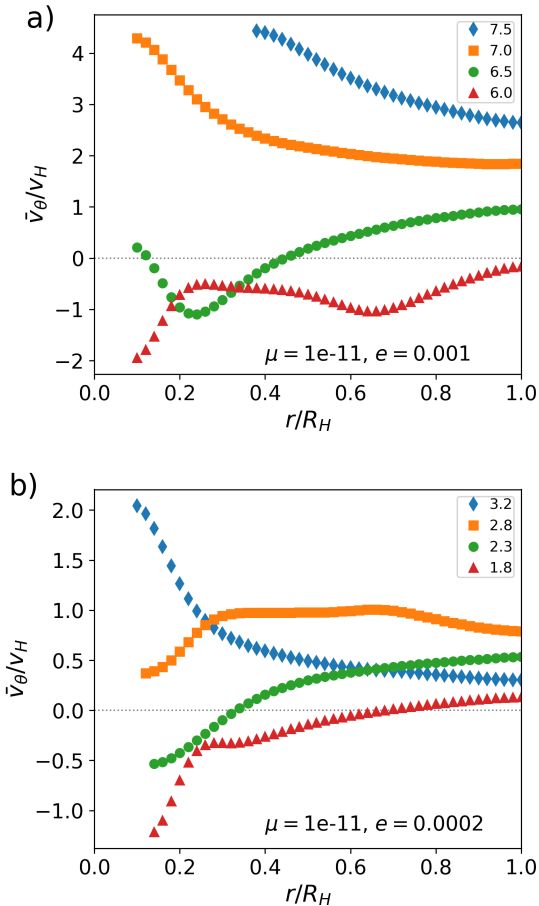
17

Figure 12: The average value of the tangential velocity component $\bar{v}_\theta$ integrated over the accretion stream for 4 different initial test particle semi-major axis values. Initial semi-major axes Δa in units of R_H are labelled in the keys. The mean velocity is measured as a function of radius from the moon's center of mass (the x axis) and is in units of the Hill radius. The mean velocity is given in units of the Hill velocity (the y axis). The points were measured from the orbits that are also shown in Figures 10 and 11. a) For moon orbital eccentricity $e = 0.001 \approx 7.1e_H$. b) For moon orbital eccentricity $e = 0.0002 \approx 1.3e_H$.

semi-major axes. The initial orbital semi-major axes (described by offset Δa) are the same as used in Figures 10 – 12 and are labelled on the lower left of each panel in units of Hill radius. In Figure 13a,c the body core remains at a fixed angle with respect to the moon/planet line which is the vertical direction. In Figure 13b,d the entire body remains tidally aligned, keeping principal body axis aligned with the moon/planet line. Figures 13a,b are for a moon with orbital eccentricity $e = 0.001 \approx 7.1e_H$ and Figures 13c,d are for a moon with orbital eccentricity $e = 0.0002 \approx 1.4e_H$.

As described in section 4.1, the center of mass position is computed after each parcel of mass is added. For Figure 13b and d, body principal axes are recomputed between each body accretion event, so as to maintain tidal alignment. We have neglected the change in the tidal orientation direction in the moon's orbit known as the librational tide since the orientation angle change would be approximately the same size as the orbital eccentricity and negligible.

The distributions of accreted material in Figure 13a and Figure 13b are similar. Pan's core is sufficiently elongated that the accreted mass does not cause a large shift in the body orientation. The mass in Pan's lobes seem to increase in with increasing western longitude, and the accreted wedges in Figures 13a,b exhibit the same trend. This suggests that the shape of the lobes on Pan's equatorial ridge is related to the angular distribution of impacting material. At lower orbital eccentricity, Figures 13a,b show more complex morphology that we attribute to the two lobes of the accretion stream that are seen in Figure 10b and 11b, particularly at larger $|\Delta a|$.

In this section we have looked at test particles in initially circular orbits originating outside the moon's orbit that impact a moon in an eccentric orbit. With test particles originating inside the moon's orbit, similar phenomena is observed after rotation by 180° about the moon center of mass. We have also integrated test particle orbits that were initially on eccentric orbits that impact a moon that is in a circular orbit. Similar orbit loops are observed for these if the same eccentricity is used for the test particle orbits when doing the comparison. This similarity was also reported by Weiss et al. (2009). In other words, we compared orbits of test particles with orbital eccentricity 0.001 impacting a moon on a circular orbit to orbits of test particles on circular orbits impacting a moon with orbital eccentricity $e = 0.001$.

In summary, for a moon in eccentric orbit with eccentricity $e > e_H$ or $e \sim e_H$, test particles in initially circular orbits have a different distribution of impact angles than those encountering a moon in a circular orbit. Test particles at the same initial semi-major axis, but different initial orbital longitudes impact the moon at different longitudes on the moon's equator. For moon orbital eccentricity $e > e_H$, particles initially exterior to the moon's orbit tend to impact the moon on the trailing side. The angular distribution of impacts peaks nearer the sub-Saturn
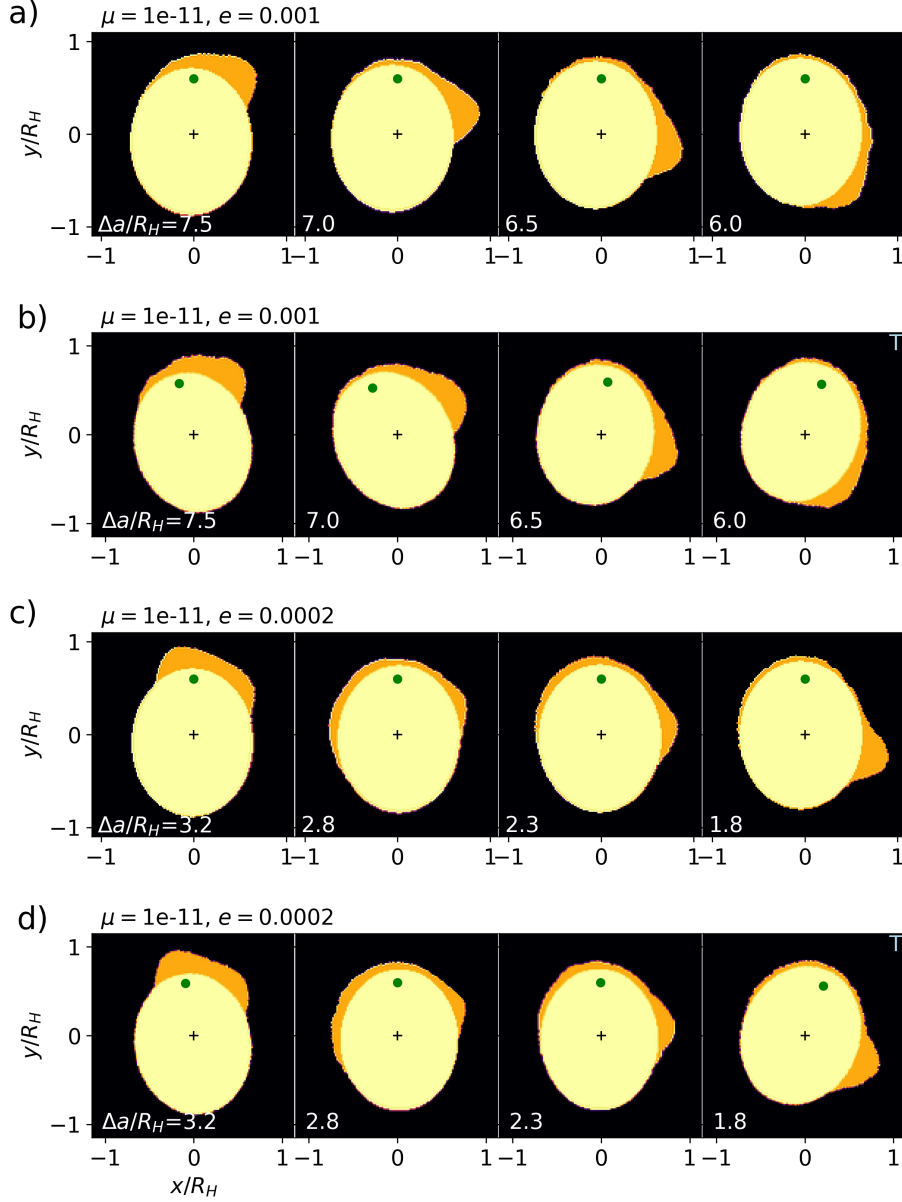
Figure 13: The distribution of accreted mass for a moon in an eccentric orbit. The moon mass ratio is $\mu = 10^{-11}$. Each row of panels shows material accreted from ring material initially in circular orbits at four different values of initial orbital semi-major axis with initial test particle semi-major axis offset $\Delta a/R_H$ labelled on the lower left of each panel. The total amount of accreted material is the same in all panels and is shown in orange. The density distributions constructed from the orbits shown in Figure 11 were used to model the longitude distribution of accreted mass. The underlying core is shown in yellow and has $b_{\mathrm{core}}/a_{\mathrm{core}} = 0.83$ and $a_{\mathrm{core}} = 0.8R_H$, based on the shape model for Pan by Thomas and Helfenstein (2020). Axes are in units of Hill radius. Panels with a 'T' in the top right corners are tidally locked orientations. a) The moon's core remains fixed during accretion and the moon's orbital eccentricity is $e = 0.001$. b) The moon remains tidally locked during accretion and the moon's orbital eccentricity is $e = 0.001$. c) The moon's core remains fixed during accretion and the moon's orbital eccentricity is $e = 0.0002$. d) The moon remains tidally locked during accretion and the moon's orbital eccentricity is $e = 0.0002$.

19

point for lower initial semi-major axis, Δa external to the moon's orbit. For $e \sim e_H$, the accretion stream can have two lobes, one impacting on the trailing side and the other on the leading side. Pan's equatorial ridge lobes seem to increase in radius with increasing western longitude, and accreted wedges constructed using the angular distribution computed from impacting orbits originating at a single initial orbital semi-major axis exhibit the same trend for $e > e_H$, but can have more complex shapes if $e \sim e_H$.

5.2. Accreting from a gap edge

In the previous section we examined accretion from a ring of disk material that originates from a single initial orbital semi-major axis. We now consider accretion from a multiple orbital semi-major axes, mimicking accretion from a gap edge that would be described by a mass surface density profile $\Sigma(\Delta a)$.

To mimic accretion from an outer edge of a gap, the accreted mass distributions in Figure 13a or c are combined after they have been multiplied by $\Sigma(\Delta a) f_a$ to take into account the gap edge mass surface density profile and the fraction of particles f_a, at each initial orbital semi-major axis, that impact the moon. The fractions of impacting particles are labelled on Figure 11. For moon eccentricity $e = 0.0002$, the fraction of particles that impact is two to three times higher at semi-major axis offset $\Delta a/R_H = 1.8$ than at the higher values (2.3, 2.8 and 3.2). For moon eccentricity $e = 0.001$, the fraction of particles that impact is about twice as high at $\Delta a/R_H = 6.0$ than at 7.5. The impact fractions increase with decreasing Δa, opposite to the drop expected in the density $\Sigma(\Delta a)$ in an outer gap edge. This would decrease the contrast between summed distributions.

In Figure 14 we show accreted mass distributions constructed from the density distributions shown in Figure 11 and 13. Each panel uses distributions from the four different initial test particle semi-major axes also shown in these figures. The equatorial ridges were accreted onto an underlying core with $b_{core}/a_{core} = 0.83$ and $a_{core} = 0.8R_H$, as previously used in Figure 13. While accreting, the body principal axis remains aligned vertically, to mimic tidal lock. For Figures 14 a,b, we use the density distributions for moon eccentricity $e = 0.001 \approx 7.1e_H$ and for Figures 14 c,d we use those for $e = 0.0002 \approx 1.4e_H$. To mimic accretion from the inner edge of a gap, we use the density distributions constructed for the outer edge and rotate the accretion stream and angular distributions by 180°.

In Figure 14 a,c the moon accretes only from an outer gap edge and with $\Sigma(\Delta a) f_a$ assumed to be constant at each of the four Δa values used to compute the angular distribution of accreting material. In Figure 14 b,d, in addition to accretion from an outer gap edge, accretion is also from an inner gap edge, but the distance to the inner edge is wider and accretion is allowed only from the outermost two semi-major axes present in Figure 11a or b.

For moon orbital eccentricity $e > e_H$, accretion from gap edges gives a fairly smooth equatorial ridge. If the inner gap edge is more distant from the moon and the outer gap edge profile is flatter than the inner gap edge profile, (Figure 14b) then the equatorial ridge has a depression on the leading side, like that of Atlas. Charnoz et al. (2007) suggested that the leading/trailing asymmetry of Atlas's equatorial ridge was due to its orbital eccentricity. However, we and Weiss et al. (2009) find that near a moon on an eccentric orbit, test particle orbits originating interior to a gap resemble those originating exterior to a gap after rotation by 180°. The leading/trailing symmetry of Pan's equatorial ridge could be due to an asymmetry in the outer and inner gap edge density profiles. We found that the leading side would accrete less for a moon in a circular orbit if the outer gap edge were more distant from the moon's orbit (see section 4.2). With moon eccentricity $e > e_H$, we find the opposite is required to match Atlas, the inner gap edge must be more distant from the moon.

Figure 13c is interesting as a sum of the different distributions in each panel would not produce an even longitude distribution. The $\Delta a/R_H = 1.8$ panel (the rightmost panel in Figure 13c) shows accreted mass concentrated at a longitude of approximately 300° W (on the lower right) and near where Pan shows a lobe in its equatorial ridge on its trailing side. The middle two panels (with $\Delta a/R_H = 2.8$ and 2.3) have wider longitude distributions of accreted material. If the mass surface density profile of the gap's outer edge extends to $\Delta a/R_H = 1.8$ then the equatorial ridge might gain a lobe at about 300° W. When we combine the angular distributions at 4 different semi-major axes and for moon eccentricity $e = 0.0002$ (see Figures 14c,d), the equatorial ridge has more structure than at higher eccentricity (Figures 14a,b). Figure 14d allowing accretion from both outer and inner gap edges but with a wider inner gap, exhibits multiple lobes with peaks, like on Pan. We see more lobate structure at $e \sim e_H$ than at $e > e_H$. This is likely because loops in the orbit (as seen in the moon's frame) are about the same size as the Hill radius when $e \sim e_H$ whereas they are larger than the Hill radius when $e > e_H$. The ridge in Figure 14d is perhaps similar to the ravioli shape of Pan's equatorial ridge. During equatorial ridge accretion, the gap profile and orbital eccentricity need not be fixed. With a varying gap profile and eccentricity, more complex shaped equatorial ridges might be accreted.

In summary, we find that an equatorial ridge with complex morphology might be accreted from ring material located in the edges of a gap, if the moon has an orbital eccentricity. A smooth equatorial ridge with a depression on the leading side, might arise if accretion took place at moon orbital eccentricity $e > e_H$ and a gap that is wider inside the moon's orbit than outside it. A multiple lobed equatorial ridge, resembling that of Pan, could be accreted at $e \sim e_H$, also with an asymmetric gap surface density profile.
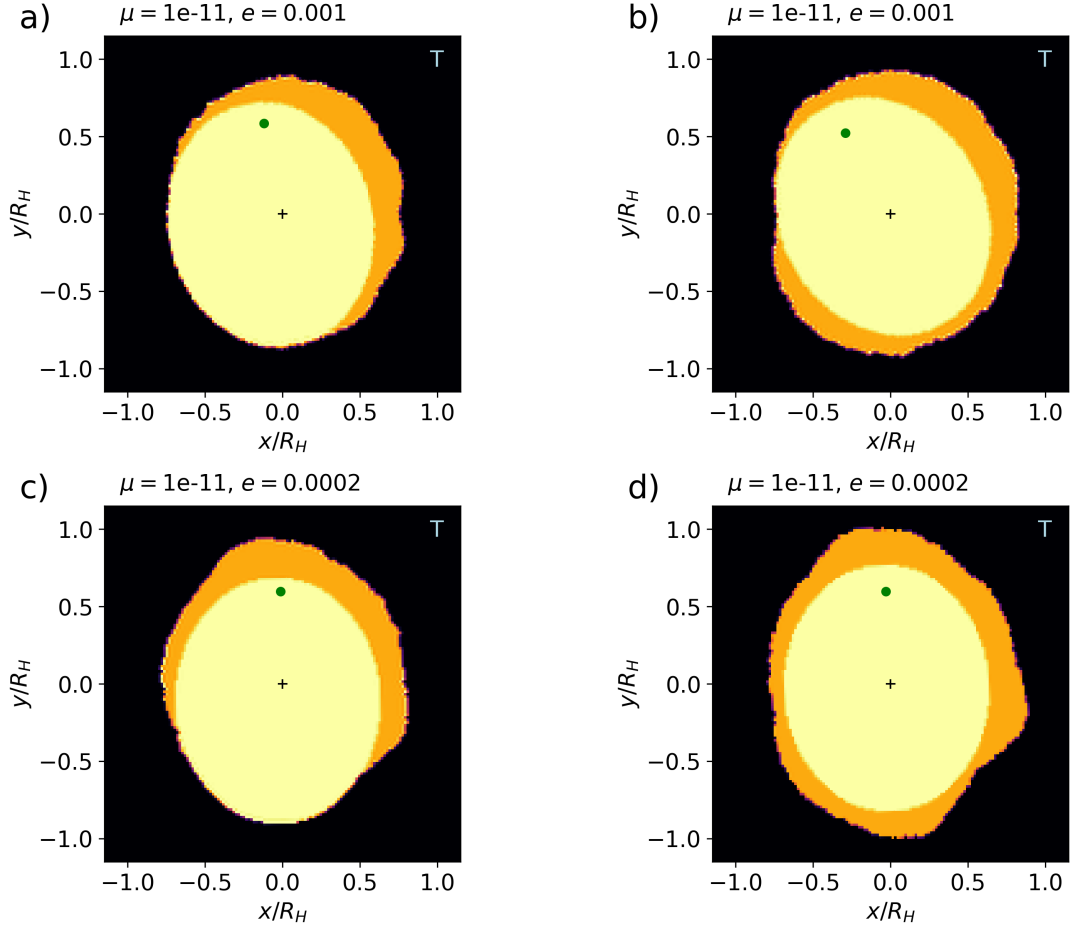
Figure 14: The distribution of accreted mass for a moon in an eccentric orbit and with roughly simulated gap profiles. The moon mass ratio is $\mu = 10^{-11}$. The total amount of accreted material is the same in all panels and is shown in orange. The density distributions constructed from the orbits and shown in Figure 11 were used to model the longitude distribution of accreted mass. The underlying core is shown in yellow and has $b_{\mathrm{core}}/a_{\mathrm{core}} = 0.83$ and $a_{\mathrm{core}} = 0.8 R_H$. Axes are in units of Hill radius. In all cases the accreting moon remains oriented as if it were tidally locked, denoted with a 'T' on the top right corners of the panels. a) The moon only accretes from its outer disk edge and the moon's orbital eccentricity is $e = 0.001$. b) The moon accretes from its outer disk edge and with a wider gap from its inner disk edge. The moon's orbital eccentricity is $e = 0.001$. c) The moon only accretes from its outer disk edge and the moon's orbital eccentricity is $e = 0.0002$. d) The moon accretes from its outer disk edge and with a wider gap from its inner disk edge. The moon's orbital eccentricity is $e = 0.0002$.

6. Scenarios for accreting equatorial ridges

A number of possible scenarios are suggested by the illustrations we have constructed showing the distribution of accreting material estimated from impacting orbits. With both moon and ring material on circular orbits, and a fixed distance between ring edge and moon semi-major axis, a multiple lobed equatorial ridge, like Pan's, probably cannot be accreted onto a tidally locked moon. We consider the following scenarios that relax the aforementioned restrictions:

- The moon's orbital eccentricity is increased due to an impact, pushing it into ring material.

- The moon is captured into a spin-orbit resonance and accretes while in this resonance.

- The moon's eccentricity is increased due to orbital resonance with another moon and its eccentricity pushes it into the ring so that it can accrete.

- The moon migrates through the ring. The migration itself maintains a narrow gap between ring edge and moon, facilitating accretion.

6.1. An impact causes an increase in orbital eccentricity

We first consider an impact mediated scenario. An impact could vary both moon orbital eccentricity and spin simultaneously; however, the eccentricity must be maintained over about 10^5 years for the accretion to take place slowly enough to satisfy the constraint on the accretion rate ensuring tidal lock, $\dot{M} < \dot{M}_{cr}$, from equation 6. Recall that if the moon starts spinning while accreting, the accreted material would be more evenly distributed and would probably lack lobes, peaks, divots or other longitudinal substructures. As discussed in section 3, the estimated eccentricity damping time due to excitation of spiral density waves is only a few thousand years, so is shorter than the required accretion time, except possibly for Atlas which is in a lower ring density region outside the A-ring. The time to regain tidal lock is 10^5 to 10^6 years (see Table 2), so the orbital eccentricity would be damped before the moon regains tidal lock. If orbital eccentricity is required to give the moon a source for ring material to accrete, then its rapid damping presents a problem for an impact triggered scenario.

6.2. Spin-orbit resonance

We consider a scenario where the moon spends time in a spin-orbit resonance. If Pan were captured into a spin-orbit resonance, instead of accreting along a single angle, material might impact at multiple angles on the body. Pan's current angular rotation rate is about 0.38 times the centrifugal break-up spin value for an equivalent density sphere, so Pan cannot spin more than three times faster than its mean motion. It could enter the 1:2 spin orbit resonance where the body rotates once every two

orbits. To enter a spin-orbit resonance, the moon must first be pulled out of tidal lock. This could happen because of an impact or a high enough accretion rate. Once a moon is pulled out of tidal lock, it must tumble prior to reaching the spin synchronous state (Wisdom, 1987) or being captured into a spin-orbit resonance.

To mimic accretion within spin-orbit resonance, we can consider a model where accretion takes place at impact angle θ_a but is consecutively rotated by an integer fraction of 2π between each mass accretion event. Because accretion occurs at symmetrical points around the equator, the orientation of the body principal axes should not change significantly during accretion. If there is structure in the accreted lobes, they must be present in the accretion stream as body orientation (taking into account the periodicity of the resonance) is unlikely to shift significantly during accretion.

The most recent shape model for Pan has peaks at longitudes near 0° and 180° W, on the Saturn-facing and anti-Saturn facing sides. Two additional peaks are found on the trailing side at longitudes of about 240° and 300°W. The trailing side suggests the moon equatorial ridge is a six-peaked polygon. However, the most recent shape model Thomas and Helfenstein (2020) (shown in silhouette in Figure 4) exhibits only a single peak on the leading side at about 100°W, instead of two peaks. This lack of symmetry implies that a spin-orbit resonance is not a good explanation for Pan's polygon-shaped equatorial ridge. Scenarios for accreting complex equatorial ridges involving spin-orbit resonance for Pan's complex equatorial ridge seem to be excluded.

6.3. Accretion due to excitation of moon orbital eccentricity by orbital resonance

We consider scenarios where a moon's eccentricity is excited due to orbital resonance with another moon. With an increase in orbital eccentricity, the moon could graze the edges of its hosting gap in the rings at orbital apocenters and pericenters, where it could accrete ring material. Epochs of moon migration, even on the slow viscous migration timescale, could push moons into pairwise orbital resonances. Migration can occur in either direction, so a moon's orbital semi-major axis can approach that of another moon leading to resonance capture and causing an increase in orbital eccentricity. While captured in a mean motion resonance, orbital eccentricity can be maintained or increased if migration continues. This mitigates the short eccentricity damping timescale discussed in section 3. The outer region of the A-ring, in which Pan and Daphnis reside, is particularly rich in first-order Lindblad resonances with Pan, Atlas, Prometheus, Pandora, Janus, Epimetheus, and Mimas (Tajeddine et al., 2017a), and Atlas's eccentricity is currently enhanced due to orbital resonance with Prometheus (Cooper et al., 2015). Small movements in the moon semi-major axes could bring two bodies into resonance.

While a moon's orbital eccentricity can be maintained by orbital resonance, in the absence of migration, a gap hosting the moon would widen. Would the gap become sufficiently wide that accretion ceases, or can accretion be maintained long enough to accrete an equatorial ridge? A moon embedded in a ring causes radial variations on the edges of its gap (Showalter, 1991; Porco et al., 2005; Porco et al., 2007; Weiss et al., 2009). A close encounter with the moon causes a change in a ring particle's semi-major axis ΔX that has been used to estimate the torque on the ring material that pushes the ring away from the moon (Goldreich and Tremaine, 1982; Weiss et al., 2009).

If the moon is on an eccentric orbit then the edge particle's shift ΔX depends on the phase of the encounter (Weiss et al., 2009). The total torque exerted on the disk material, integrated over ring longitude, may not be strongly dependent on the moon's eccentricity (Goldreich and Sari, 2003). However the orbit integrations by Weiss et al. (2009) suggest that locations or distances from the moon's semi-major axis where the torque is exerted onto the ring material could depend on eccentricity. The torque from the moon onto the ring is probably exerted onto the disk over a larger range in semi-major axis offset Δa if the moon is on an eccentric orbit, than if the moon is on a circular orbit. Unfortunately, predictions of gap surface density profiles that balance the torque caused by the moon onto the ring against viscous diffusion and accretion usually assume the moon is in a circular orbit (Grätz et al., 2019). This is usually a good assumption because of the short eccentricity damping time (as we discussed in section 3). So far as we know, gap edge surface density profiles for gaps opened by eccentric moons have not been predicted analytically.

Moons are characterized as able to open a gap or not, depending upon the moon mass ratio and viscosity in the disk (Lissauer et al., 1981). An eccentricity of a few e_H would let Pan or Daphnis graze their gap edges. If the torque exerted on the ring material is not a strong function of orbital eccentricity and the eccentricity is maintained due to orbital resonance with another moon, then the gaps opened by Pan or Daphnis would not be wide enough to stop accretion. As long as the moon eccentricity can be maintained, accretion via grazing gap edges would seem to be a viable scenario for accretion of an ornamental equatorial ridge.

6.4. Accreting while undergoing radial migration

We consider equatorial ridge accretion scenarios involving a migrating moon. An advantage of a migration scenario is that proximity of dense and cold ring material to the moon can be prolonged by the migration itself. With little or no migration, ring material is pushed away from the moon's orbit and its hosting gap widens due to scattering and torques associated with spiral density waves that are driven by the moon itself. The gap widens until spiral density wave driven torques balance those associated with viscous spreading and an equilibrium state is achieved. The Keeler and Encke gaps are wide enough to prevent accretion onto Daphnis and Pan, though Pan's gap is not entirely empty (Hedman et al., 2013). If the moon migrates quickly, it can remain in proximity to ring material or only open a narrow gap (see Figure 4 by Bromley and Kenyon 2013 showing an N-body simulation of a moon rapidly migrating into a particulate disk). The gap of a migration moon can be asymmetric and contain substructures such as feathers (Weiss et al., 2009) or streams (Figure 4 by Bromley and Kenyon 2013). In section 4.2 and 5.2, we found that accretion from a gap that has asymmetric surface density edge profiles might account for Pan and Atlas' equatorial ridge morphology. Migration might naturally cause a difference between the density profile of the gap edge that the moon is migrating toward compared to the one on the opposite side.

Pan, Daphnis and Atlas are too massive to migrate via the type I migration mechanism where the body remains embedded within the ring material (Bromley and Kenyon, 2013). If they opened a gap and migrated via a type II mechanism and at the viscous evolution rate (about 10^{-6} km/yr, eqn 28 by Bromley and Kenyon 2013), then little ring material would have been near enough to the moon to accrete onto it. The type III migration mechanism (Masset and Papaloizou, 2003) requires ring material to pass near the moon (Ida et al., 2000; Masset and Papaloizou, 2003), so accretion onto the moon could be a natural consequence of this mechanism. Bromley and Kenyon (2013) estimate that both Pan and Daphnis could undergo rapid migration, at a semi-major axis drift rate of about $\frac{da_{\mathrm{mig}}}{dt} \sim 20$ km/yr, and in the mode of type III migration where corotating material is gravitationally pulled from one side of the orbit to the other (Ida et al., 2000; Masset and Papaloizou, 2003). Estimates of the type III migration rate are based on the moon/particle encounter frequency in the moon's corotation zone and so proportional to the ring mass surface density, Σ_{ring} (Ida et al., 2000; Bromley and Kenyon, 2013).

In section 2.2 we estimated that the duration of equatorial ridge accretion was at least 10^5 years. An issue with a rapid migration rate of 20 km/yr is that in 10^5 yr, the moon could pass entirely through Saturn's rings. However, type III radial migration can go in either direction, inward or outward, depending upon how it is triggered (Bromley and Kenyon, 2013). Type III migration requires a cold particulate disk and is prevented or slowed by inclination and eccentricity excitation of particles in the ring. As the A-ring exhibits variations in density with abrupt transitions or jumps at the locations of gaps and resonances (Tajeddine et al., 2017a; Tiscareno and Harris, 2018), a migrating moon would likely experience variations in migration rate. If migration can be slower at times and with reversals, then perhaps Atlas, Pan and Daphnis could have experienced episodic events of fast migration.

How much ring mass passes through the moon's orbit per unit time during type III migration? We can estimate

this rate from the migration rate and ring surface density

$$\dot{M}_{\mathrm{cross}} = 2\pi a \frac{da_{\mathrm{mig}}}{dt} \Sigma_{\mathrm{ring}}$$
$$= 3 \times 10^{14} \text{ kg/yr} \left(\frac{a}{a_{Pan}}\right) \left(\frac{da_{\mathrm{mig}}/dt}{1 \text{ km/yr}}\right) \left(\frac{\Sigma_{\mathrm{ring}}}{400 \text{ kg m}^{-2}}\right)$$
$$(11)$$

The accretion rate onto the moon would be a fraction of this mass rate, $\dot{M} = f_a \dot{M}_{\mathrm{cross}}$ where we relate the two rates with an accretion efficiency f_a.

In section 2.2 we estimated that accretion must remain below a critical accretion rate $\dot{M}_{cr} \sim 2 \times 10^{10}$ km/yr for Pan, to maintain tidal lock (otherwise the equatorial ridge would be evenly distributed about the equator). Using equation 11 we estimate the critical accretion efficiency $f_{a,cr}$ that gives the critical accretion rate $\dot{M}_{cr}$ onto the moon,

$$f_{a,cr} = \frac{\dot{M}_{cr}}{\dot{M}_{\mathrm{cross}}}$$
$$\sim 3 \times 10^{-5} \left(\frac{\dot{M}_{cr}}{10^{10} \text{ kg/yr}}\right) \left(\frac{1 \text{ km/yr}}{da_{\mathrm{mig}}/dt}\right) \left(\frac{400 \text{ kg m}^{-2}}{\Sigma_{\mathrm{ring}}}\right)$$
$$(12)$$

If the migration rate is only about 1 km/s (which would allow the moon to stay in the rings longer) then the accretion efficiency would be similar to the $f_a \sim 10^{-4}$ we measured for particles accreting from a ring near an eccentric planet per orbit (shown in each panel in Figure 11). In a migrating moon scenario for equatorial ridge accretion, there would be a relation between accretion efficiency, the gap edge profiles, the migration rate, the disk density and the impact angle distribution of accreting material. Orbital resonances with other moons would also affect these quantities. If migration is not steady then as a consequence we expect variations in the angular distribution of accreting material. Such variations might account for some of the morphology, such as thickness variations or narrow streaks that are present on Pan's equatorial ridge.

A problem with the migration scenario for equatorial ridge accretion is that for moon and ring particles in circular orbits, we did not find an explanation for the multiple lobes on Pan's equatorial ridge (see section 4). Accretion from an asymmetric gap while on an eccentric orbit is more likely to account for Pan's ravioli-shaped ridge (explored in section 4.2). Eccentricity damping while migrating is expected to be rapid (Rein and Papaloizou, 2010; Bromley and Kenyon, 2013). However, if orbital resonances with other moons are encountered during migration then perhaps migration and eccentricity excitation could be concurrent. Eccentricity excitation from orbital resonance would require some migration, and while migration is taking place, orbital resonances would be encountered. So it may not be possible to cleanly separate or differentiate between these two scenarios.

Up to this point we have neglected Daphnis. The images of Daphnis shown in Figure 1 suggest that Daphnis is elongated or nearly prolate. However, the body axis ratios and silhouettes by Thomas and Helfenstein (2020) of Daphnis are not significantly different than those of Atlas. Daphnis has a second ridge that is at a latitude of about 22° N, centered at about 80° W and extends about $\sim 90°$ in longitude (Buratti et al., 2019; Thomas and Helfenstein, 2020). This second ridge could have been accreted while the moon was tilted with respect to the orbital plane. If the moon were nearly prolate, it would more easily reorient itself by rotating about its long axis while accreting. We have explored how the moon can slowly tidally realign by rotating in the equatorial plane while accreting. If Daphnis were nearly prolate, perhaps it could also roll or vary in obliquity during accretion.

In summary, we have excluded impact and spin-orbit resonance related scenarios for accretion of ornamental equatorial ridges. Scenarios involving moon migration and eccentricity excitation are promising. A type III migration-mediated mechanism for equatorial ridge accretion has the advantage that material must cross the gap for migration to take place, the gap hosting the moon would be narrower, facilitating accretion, and the gap would probably be asymmetric, facilitating accretion of asymmetric equatorial structures. However, accretion of multiple lobes seems to require moon orbital eccentricity which is usually rapidly damped during migration. Eccentricity excitation due to orbital resonance with another moon could force a moon into a gap edge, facilitating accretion; however, we are not sure if the gap would remain sufficiently narrow for accretion to continue for the required accretion duration of $\sim 10^5$ years. To put these moons into orbital resonance, some migration is needed, and during an epoch of migration, orbital resonances might be encountered that would increase orbital inclination and eccentricity and slow the migration. These two scenarios are probably connected.

7. Summary and Discussion

We have estimated a critical accretion rate, $\dot{M}_{cr}$ that would be large enough to pull a moon out of a tidally locked state or a spin-orbit resonance. If the moon is not tidally locked (or in a spin-orbit resonance) then we would expect accretion to be evenly distributed around the equator giving a ridge that lacks divots, depressions or multiple peaks. As Pan and Atlas's ridges have non-axisymmetric structures, we infer that the accretion rates of their ridges primarily occurred at rates below $M_{cr} \sim 10^{10}$ kg/yr. From the volume in their equatorial ridges, we infer that the duration of accretion was at least 10^5 years.

Integration of test particles on initially circular orbits shows that only particles with orbital semi-major axes satisfying $1.7 \lesssim |\Delta a|/R_H \lesssim 2.5$ are likely to impact a moon on a circular orbit upon their first close approach. We find that particles can impact the moon's surface at almost any longitude on the moon's equator.

We explored a tidal accretion model that takes into account body shape changes while maintaining tidal alignment. If the accretion angle is within about 45° of the sub-planet or anti-planet line, the moon can slowly rotate while it accretes due to tidal realignment and giving wedge-shaped lobes on the equatorial ridge. Integrated orbits show a nearly linear relation between impact angle and test particle initial orbital semi-major axis. A moon accreting from an external gap edge would accrete more mass at larger western longitudes on its equator and this too can give a wedge-shaped equatorial lobe, but in this case the slope (or derivative of radial extent with respect to longitude) of an accreted wedge is related to the surface density profile of ring material in the gap edge.

For a moon in eccentric orbit, with eccentricity $e > e_H$ or $e \sim e_H$ (where e_H is the Hill eccentricity), test particles in initially circular orbits at a single semi-major axis have a wide distribution of possible impact angles. Particles initially exterior to the moon's orbit tend to impact the moon on the trailing side. Their impact longitude distribution peaks nearer the sub-Saturn point for test particles with initial orbital semi-major axis nearer that of the moon, or with lower $|\Delta a|$. For moon orbital eccentricity $e \sim e_H$, the accretion stream can have two lobes, one impacting on the trailing side and the other on the leading side.

Multiple lobes, like those on Pan's equatorial ridge, might be accreted from an asymmetric gap and at orbital eccentricity $e \sim e_H$. A depression on the moon's leading side, such as present on Atlas's ridge, could be due to accretion from an asymmetric gap, either at low eccentricity and with a wider gap exterior to the moon's orbit, or at $e > e_H$ and with a wider gap interior to the moon's orbit.

We exclude impact and spin-orbit resonance related scenarios for accretion of ornamental equatorial ridges. A type III moon migration-mediated mechanism for equatorial ridge accretion has the advantage that material must cross the gap for migration to take place, the gap hosting the moon would be narrower, facilitating accretion, and the gap would be asymmetric, facilitating accretion of asymmetric equatorial structures. Eccentricity excitation due to orbital resonance with another moon could push a moon into a gap edge, facilitating accretion, however the gap may widen afterward, cutting off accretion. A scenario for accretion while in orbital resonance has the advantage that the orbital eccentricity might be maintained for the required 10^5 year duration, otherwise eccentricity would be damped rapidly by driving spiral density waves (Hahn, 2008; Rein and Papaloizou, 2010; Bromley and Kenyon, 2013). To enter orbital resonance with another moon, some migration is needed, and during an epoch of migration, orbital resonances would be encountered and possibly maintained. These two scenarios are probably connected. Migration, eccentricity and inclination excitation could be concurrent.

In this study we have considered orbits near point masses, and neglected collisions between accreting particles, scattering upon impact, and mass redistribution on the moon's surface or in the accreted ridge interior. We assumed that the accretion stream originates from material in nearly circular orbits, which would be a reasonable approximation in a quiescent high opacity ring. Future studies could study the role of the complex local gravity field and collisions between particles that could occur in the accretion stream. We primarily looked at orbits in the equatorial plane, but the inclination distribution of ring particles affects the thickness of accreted equatorial ridges (Charnoz et al., 2007) and could also affect the migration rate (Bromley and Kenyon, 2013). As test particles were begun in circular orbits we have neglected the role of waves in ring edges (Cuzzi and Scargle, 1985; Weiss et al., 2009) that might be correlated with the phase of the moon in its orbit. These too would affect the angular distribution of impacts on a moon's surface. We have neglected rotational tilt and libration of the moon that might be excited during accretion. Because impact craters are visible on Pan and Atlas's equatorial ridges (Buratti et al., 2019), we have assumed that accretion was higher in the past. However, the Encke gap is not empty (Hedman et al., 2013), so accretion could be ongoing, but at a low rate.

The N-body simulations of equatorial ridge accretion by Charnoz et al. (2007) lacked collisions between ring particles and were run only for about 10^4 orbits. As accreting ring particles were massless, migration did not take place. These numerical issues affect the gap density profile and the orbital eccentricity and inclination of distributions of particles in the gap edges, and as a consequence, the latitude and longitude distribution of the simulated impacts on the moon. The N-body simulations by Bromley and Kenyon (2013) showed type III migration but did not track the near moon environment to follow equatorial ridge growth. Neither set of simulations included additional moons that could excite orbital resonances. It would be interesting to carry out more complex and sophisticated simulations that might test some of our speculations on equatorial ridge growth.

Table 1: Moon measured properties

Quantity	symbol	units	Pan	Daphnis	Atlas
Orb. semi-major axis	a	R_S	2.22	2.26	2.29
Orb. Eccentricity	e		$1.44 \pm 0.54 \times 10^{-5}$	$3.31 \pm 0.62 \times 10^{-5}$	0.012
Orb. Inclination	i	degrees	$1 \pm 4 \times 10^{-4}$	$3.6 \pm 1.3 \times 10^{-3}$	3.1×10^{-3}
Orb. Rotation period	P	days	0.575	0.594	0.602
Mass	M	10^{16} kg	0.495	0.0077	0.66
Density	ρ	kg m^{-3}	400 ± 31	276 ± 144	412 ± 19
Mean body radius	R_m	km	13.7 ± 0.3	3.9 ± 0.5	14.9 ± 0.2
Body semi-major axis	a_{body}	km	17.3 ± 0.2	4.9 ± 0.3	20.4 ± 0.1
Body semi axis	b_{body}	km	14.1 ± 0.2	4.2 ± 0.8	17.7 ± 0.2
Body semi-minor axis	c_{body}	km	10.5 ± 0.5	2.8 ± 0.6	9.3 ± 0.3
Volume fraction	f_v	%	10	1	25
Core axis ratio	$c_{\text{core}}/a_{\text{core}}$		0.65		0.54
Core axis ratio	$c_{\text{core}}/b_{\text{core}}$		0.78		0.58
Core axis ratio	$b_{\text{core}}/a_{\text{core}}$		0.83		0.93

Notes: Here $R_S = 60268$ km is the equatorial radius of Saturn. The mass for Atlas is taken from Jacobson et al. (2008) and those for Pan and Daphnis from Porco et al. (2007). Orbital elements are by Jacobson et al. (2008). Mean density ρ, mean radius R_m, body semi axes $a_{\text{body}}, b_{\text{body}}, c_{\text{body}}$ volumes of the equatorial ridges divided by total moon volume, f_v, are by Thomas and Helfenstein (2020). Core axis ratios are estimates of the body axis ratios after removing the equatorial ridge and also by Thomas and Helfenstein (2020). We omit these for Daphnis as the volume fraction in its ridges is small.

Table 2: Moon computed properties

	symbol	units	Pan	Daphnis	Atlas
Hill radius	R_H	km	19.09	4.85	21.02
Hill velocity	v_H	m/s	2.4	0.6	2.5
Hill eccentricity	e_H		1.4×10^{-4}	3.6×10^{-5}	1.5×10^{-4}
Ratio of fill	a_{body}/R_H		0.91	1.01	0.97
Time to spin down	t_{despin}	yr	9×10^4	1×10^6	9×10^4
Time to spin down	t_{despin}/P		6×10^7	9×10^8	6×10^7
Accretion to tidal torque ratio	$\frac{T_{\text{acc}}}{T_2}\frac{Mn}{\dot{M}}$		10^9	10^{10}	10^9
Critical accretion rates	$\dot{M}_{cr}$	kg/yr	2×10^{10}	2×10^7	3×10^{10}
Critical accretion time scale	$M f_v/\dot{M}_{cr}$	yr	2×10^4	4×10^4	6×10^4

Notes: The Hill radius $R_H = a(M/(3M_*))^{\frac{1}{3}}$ is computed from values in Table 1. The Hill velocity $v_H = aR_H$. The Hill eccentricity $e_H = R_H/a$. The ratio of fill is the body semi-major axis divided by the Hill radius, a_{body}/R_H. Here P is the orbital period. Spin-down times are computed using shear modulus times dissipation factor $\mu_{\text{shear}}Q \sim 10^{11}$ Pa and equation 2. The ratio of accretion to tidal torque $\frac{T_{\text{acc}}}{T_2}\frac{Mn}{\dot{M}}$ is computed using equation 5. The critical accretion rate, $\dot{M}_{cr}$, that can pull the moon out of the spin synchronous state is estimated using equation 6.

Bibliography

References

Borderies, N., Goldreich, P., Tremaine, S., Sep. 1982. Sharp edges of planetary rings. Nature 299, 209–211.

Borderies, N., Goldreich, P., Tremaine, S., Aug. 1989. The formation of sharp edges in planetary rings by nearby satellites. Icarus 80 (2), 344–360.

Bromley, B. C., Kenyon, S. J., 2013. Migration of small moons in Saturn's rings. Astrophysical Journal 764 (2), 192.

Buratti, B. J., Thomas, P. C., Roussos, E., Howett, C., Seiss, M., Hendrix, A. R., Helfenstein, P., Brown, R. H., Clark, R. N., Denk, T., Filacchione, G., Hoffmann, H., Jones, G. H., Khawaja, N., Kollmann, P., Krupp, N., Lunine, J., Momary, T. W., Paranicas, C., Postberg, F., Sachse, M., Spahn, F., Spencer, J., Srama, R., Albin, T., Baines, K. H., Ciarniello, M., Economou, T., Hsu, H.-W., Kempf, S., Krimigis, S. M., Mitchell, D., Moragas-Klostermeyer, G., Nicholson, P. D., Porco, C. C., Rosenberg, H., Simolka, J., Soderblom, L. A., 2019. Close Cassini flybys of Saturn's ring moons Pan, Daphnis, Atlas, Pandora, and Epimetheus. Science 364, 1053.

Charnoz, S., Brahic, A., .Thomas, P. C., Porco, C. C., 2007. The equatorial ridges of Pan & Atlas: Terminal accretionary ornaments? Science 318 (5856), 1622–1624.

Cooper, N. J., Renner, S., Murray, C. D., Evans, M. W., 2015. Saturn's inner satellites: Orbits, masses, and the chaotic motion of Atlas from new Cassini imaging observations. Astronomical Journal 149 (1), 27.

Cuzzi, J. N., Scargle, J. D., 1985. Wavy edges suggest moonlet in Encke's gap. Astrophysical Journal 292, 276–290.

Dermott, S. F., Murray, C. D., 1981. The dynamics of tadpole and horseshoe orbits. I - Theory. Icarus 48 (1), 1–11.

Efroimsky, M., Makarov, V. V., Feb 2013. Tidal friction and tidal lagging. Applicability limitations of a popular formula for the tidal torque. Astrophysical Journal 764 (1), 26.

Frouard, J., Quillen, A. C., Efroimsky, M., Giannella, D., 2016. Numerical simulation of tidal evolution of a viscoelastic body modelled with a mass-spring network. Monthly Notices of the Royal Astronomical Society 458, 2890–2901.

Goldreich, P., 1963. On the eccentricty of satellite orbits in the solar system. Monthly Notices of the Royal Astronomical Society 126, 257–268.

Goldreich, P., Sari, R., 2003. Eccentricity Evolution for Planets in Gaseous Disks. Astrophysical Journal 585 (2), 1024–1037.

Goldreich, P., Tremaine, S., Jan. 1982. The dynamics of planetary rings. Annual Review of Astronomy and Astrophysics 20, 249–283.

Grätz, F., Seiß, M., Schmidt, J., Colwell, J., Spahn, F., Feb. 2019. Sharp Gap Edges in Dense Planetary Rings: An Axisymmetric Diffusion Model. Astrophysical Journal 872 (2), 153.

Hahn, J. M., 2008. The secular evolution of a close ring-satellite system: The excitation of spiral density waves at a nearby gap edge. Astrophysical Journal 680 (2), 1569–1581.

Hedman, M. M., Burns, J. A., Hamilton, D. P., Showalter, M. R., Mar. 2013. Of horseshoes and heliotropes: Dynamics of dust in the Encke Gap. Icarus 223 (1), 252–276.

Ida, S., Bryden, G., Lin, D. N. C., Tanaka, H., 2000. Orbital Migration of Neptune and Orbital Distribution of Trans-Neptunian Objects. Astrophysical Journal 534 (1), 428–445.

Ip, W. H., Aug. 2006. On a ring origin of the equatorial ridge of Iapetus. Geophysical Research Letters 33 (16), L16203.

Jacobson, R. A., J. Spitale, J., Porco, C. C., Beurle, K., Cooper, N. J., Evans, M. W., Murray, C. D., 2008. Revised orbits of Saturn's small inner satellites. Astronomical Journal 135, 261.

Karjalainen, R., 2007. Aggregate impacts in Saturn's rings. Icarus 189, 523–537.

Kaula, M., 1964. Tidal dissipation by solid friction and the resulting orbital evolution. Reviews of Geophysics 2, 661–684.

Leleu, A., Jutzi, M., Rubin, M., 2018. The peculiar shapes of Saturn's small inner moons as evidence of mergers of similar-sized moonlets. Nature Astronomy 2, 555–561.

Lissauer, J. J., Shu, F. H., Cuzzi, J. N., Aug. 1981. Moonlets in Saturn's rings? Nature 292 (5825), 707–711.

Masset, F. S., Papaloizou, J. C. B., 2003. Runaway Migration and the Formation of Hot Jupiters. Astrophysical Journal 588 (1), 494–508.

Ostro, S. J., Margot, J.-L., Benner, L. A. M., Giorgini, J. D., Scheeres, D. J., Fahnestock, E. G., Broschart, S. B., Bellerose, J., Nolan, M. C., Magri, C., Pravec, P., Scheirich, P., Rose, R., Jurgens, R. F., Jong, E. M. D., Suzuki, S., 2006. Radar imaging of binary near-earth asteroid (66391) 1999 KW4. Science 314 (5803), 1276–1280.

Peale, S. J., Cassen, P., 1978. Contribution of tidal dissipation to lunar thermal history. Icarus 36 (245-269).

Porco, C., Danielson, G. E., Goldreich, P., Holberg, J. B., Lane, A. L., Oct. 1984. Saturn's nonaxisymmetric ring edges at 1.95 R_s and 2.27 R_s. Icarus 60 (1), 17–28.

Porco, C. C., Baker, E., Barbara, J., Beurle, K., Brahic, A., Burns, J. A., Charnoz, S., Cooper, N., Dawson, D. D., Del Genio, A. D., Denk, T., Dones, L., Dyudina, U., Evans, M. W., Giese, B., Grazier, K., Helfenstein, P., Ingersoll, A. P., Jacobson, R. A., Johnson, T. V., McEwen, A., Murray, C. D., Neukum, G., Owen, W. M., Perry, J., Roatsch, T., Spitale, J., Squyres, S., Thomas, P., Tiscareno, M., Turtle, E., Vasavada, A. R., Veverka, J., Wagner, R., West, R., Feb. 2005. Cassini Imaging Science: Initial Results on Saturn's Rings and Small Satellites. Science 307 (5713), 1226–1236.

Porco, C. C., Thomas, P. C., Weiss, J. W., Richardson, D. C., 2007. Saturn's small inner satellites: Clues to their origins. Science 318, 1602.

Pravec, P., Scheirich, P., Ďurech, J., Pollock, J., Kušnirák, P., Hornoch, K., Galád, A., Vokrouhlický, D., Harris, A., Jehin, E., Manfroid, J., Opitom, C., Gillon, M., Colas, F., Oey, J., Vraštil, J., Reichart, D., Ivarsen, K., Haislip, J., LaCluyze, A., 2014. The tumbling spin state of (99942) Apophis. Icarus 233, 48 – 60.

Rein, H., Liu, S.-F., 2012. REBOUND: an open-source multi-purpose N-body code for collisional dynamics. Astronomy and Astrophysics 537, A128.

Rein, H., Papaloizou, J. C. B., 2010. Stochastic orbital migration of small bodies in Saturn's rings. Astronomy and Astrophysics 524, A22.

Rein, H., Spiegel, D. S., Jan. 2015. IAS15: a fast, adaptive, high-order integrator for gravitational dynamics, accurate to machine precision over a billion orbits. Monthly Notices of the Royal Astronomical Society 446 (2), 1424–1437.

Showalter, M. R., Jun. 1991. Visual detection of 1981S13, Saturn's eighteenth satellite, and its role in the Encke gap. Nature 351 (6329), 709–713.

Spitale, J. N., Jacobson, R. A., Porco, C. C., Owen, Jr., W. M., 2006. The orbits of Saturn's small satellites derived from combined historic and Cassini imaging observations. Astronomical Journal 132 (2), 692–710.

Spitale, J. N., Porco, C. C., Nov. 2009. Time variability in the outer edge of Saturn's A-Ring revealed by Cassini imaging. Astronomical Journal 138 (5), 1520–1528.

Stickle, A. M., Roberts, J. H., Jun. 2018. Modeling an exogenic origin for the equatorial ridge on Iapetus. Icarus 307, 197–206.

Tajeddine, R., Nicholson, P. D., Longaretti, P.-Y., El Moutamid, M., Burns, J. A., 2017a. What confines the rings of Saturn? Astrophysical Journal Supplements 232 (2), 28.

Tajeddine, R., Nicholson, P. D., Tiscareno, M. S., Hedman, M. M., Burns, J. A., El Moutamid, M., 2017b. Dynamical phenomena at the inner edge of the Keeler gap. Icarus 289, 80–93.

Thomas, P., Helfenstein, P., 2020. The small inner satellites of Saturn: Shapes, structures and some implications. Icarus 344, 113355.

Thomas, P. C., 2010. Sizes, shapes, and derived properties of the Saturnian satellites after the Cassini nominal mission. Icarus 208, 395–401.

Thomas, P. C., Burns, J. A., Hedman, M., Helfenstein, P., Morrison, S., Tiscareno, M. S., 2013. The inner small satellites of Saturn: A variety of worlds. Icarus 226 (1), 999–1019.

Tiscareno, M. S., Burns, J. A., Nicholson, P. D., Hedman, M. M.,

27

Porco, C. C., 2007. Cassini imaging of Saturn's rings. II. a wavelet technique for analysis of density waves and other radial structure in the rings. Icraus 189 (1), 14–34.

Tiscareno, M. S., Harris, B. E., Sep. 2018. Mapping spiral waves and other radial features in Saturn's rings. Icarus 312, 157–171.

Weiss, J. W., Porco, C. C., Tiscareno, M. S., 2009. Ring edge waves and the masses of nearby satellites. Astronomical Journal 138 (1), 272–286.

Wisdom, J., 1987. Rotational dynamics of irregularly shaped natural satellites. Astronomical Journal 94 (5), 1350–1360.

Yasui, Y., Ohtsuki, K., Daisaki, H., 2014. Gravitational accretion of particles onto moonlets embedded in Saturn's rings. Astrophysical Journal 797, 93.

Yoder, C. F., 1982. Tidal rigidity of Phobos. Icarus 49 (3), 327–346.

Appendix A. Changes to body shape and tidal alignment

We describe how we find the body principal axes in our two-dimensional accretion model. Tidal alignment is mimicked by tilting the body so that the major axis remains oriented vertically. We start with a coordinate frame with x along the long principal body axis and z along the short principal body axis. The moment of inertia matrix is diagonal

$$\mathbf{I} = \begin{pmatrix} A & 0 & 0 \\ 0 & B & 0 \\ 0 & 0 & C \end{pmatrix} \qquad (A.1)$$

with $A < B < C$.

We now consider the same body that is rotated counter-clockwise by angle ϕ in the xy plane. The moment of inertia matrix is no longer diagonal. It is convenient to define a 2-dimensional matrix

$$\tilde{\mathbf{I}} = \begin{pmatrix} I_{xx} & I_{xy} \\ I_{xy} & I_{yy} \end{pmatrix}. \qquad (A.2)$$

This same body now has xy components of the moment of inertia matrix

$$\begin{aligned} \tilde{\mathbf{I}} &= \begin{pmatrix} \cos\phi & -\sin\phi \\ \sin\phi & \cos\phi \end{pmatrix} \begin{pmatrix} A & 0 \\ 0 & B \end{pmatrix} \begin{pmatrix} \cos\phi & \sin\phi \\ -\sin\phi & \cos\phi \end{pmatrix} \\ &= \frac{A+B}{2} \begin{pmatrix} 1 & 0 \\ 0 & 1 \end{pmatrix} + \frac{A-B}{2} \begin{pmatrix} \cos(2\phi) & \sin(2\phi) \\ \sin(2\phi) & -\cos(2\phi) \end{pmatrix}. \end{aligned} \qquad (A.3)$$

The I_{zz} component of the moment of inertia matrix is unchanged by rotation in the xy plane. This relation for $\tilde{\mathbf{I}}$ can be inverted to compute the rotation angle ϕ from the components of the moment of inertia matrix,

$$\phi = \frac{1}{2}\arctan2\left(2I_{xy}, I_{xx} - I_{yy}\right). \qquad (A.4)$$

This rotation angle determines the orientation of a principal body axis in the xy plane. The unit vector $(\cos\phi, \sin\phi)$ is an eigenvector of $\tilde{\mathbf{I}}$ but it could have eigenvalue A or B. To determine the orientation of the longest body axis, we compute the two eigenvalues of $\tilde{\mathbf{I}}$ using its eigenvectors

$$\lambda_1 = \left| \tilde{\mathbf{I}} \begin{pmatrix} \cos\phi \\ \sin\phi \end{pmatrix} \right| \qquad \lambda_2 = \left| \tilde{\mathbf{I}} \begin{pmatrix} \cos(\phi + \pi/2) \\ \sin(\phi + \pi/2) \end{pmatrix} \right|. \quad (A.5)$$

The angle associated with the smaller eigenvalue gives the orientation angle of the long body axis. We use this computation to determine the orientation of a tidally aligned body.

Accretion will cause the moment of inertia matrix to vary. With accretion at a fixed angle θ_a will the body orientation ϕ increase or decrease? We take the derivative of the rotation angle ϕ with respect to changes in the components of the moment of inertia matrix

$$\delta\phi = \frac{-I_{xy}(\delta I_{xx} - \delta I_{yy}) + (I_{xx} - I_{yy})\delta I_{xy}}{4I_{xy}^2 + (I_{xx} - I_{yy})^2}. \qquad (A.6)$$

We assume that the body is tidally aligned so $\tilde{\mathbf{I}}$ is originally diagonal. Then I_{xy} vanishes, and the above equation becomes

$$\delta\phi = \frac{\delta I_{xy}}{I_{xx} - I_{yy}}. \qquad (A.7)$$

We assume that $I_{yy} < I_{xx}$ for tidal alignment of the long axis vertically.

We add mass at radius r_a and at accretion angle θ_a from vertical. The mass is added at position $(x, y) = r_a(-\sin\theta_a, \cos\theta_a)$, giving a change in the xy components of the moment of inertia matrix

$$\delta\tilde{\mathbf{I}} = \frac{dm}{2}r_a^2 \begin{pmatrix} 1 + \cos(2\theta_a) & \sin(2\theta_a) \\ \sin(2\theta_a) & 1 - \cos(2\theta_a) \end{pmatrix}. \qquad (A.8)$$

This gives a change to the orientation angle of the principal body axis

$$\delta\phi = \frac{dm}{2}r_a^2 \frac{\sin(2\theta_a)}{(I_{xx} - I_{yy})}. \qquad (A.9)$$

Since the angle adjustment depends on the difference in the diagonal components of the moment of inertia matrix it is useful to compute the change in $I_{xx} - I_{yy}$ caused by accreting the mass dm,

$$\delta(I_{xx} - I_{yy}) = dm\, r_a^2 \cos(2\theta_a). \qquad (A.10)$$

If $|\theta_a| < \pi/4$ then the difference in the eigenvalues of the moment of inertial matrix is enhanced and the body becomes more elongated. This in turn affects the size of $\delta\phi$. As mass is added, the size of the angular shift in body orientation decreases. A wedge-shaped lobe is accreted. If $|\theta_a| > \pi/4$ then the body becomes rounder and the size of the angular shift increases as mass accretes. Mass is accreted at all longitudes. These trends are for a fixed accretion radius r_a and here we have ignored its dependence on angle. For more elongated bodies, the angular shift would be smaller than estimated with an angular independent accretion radius r_a.